Mechanochemical Stress Sensing

A Correlation of Strain Field and Spiropyran Activation in Elastomers

Rodrigo Fonseca de Carvalho

Delft University of Technology

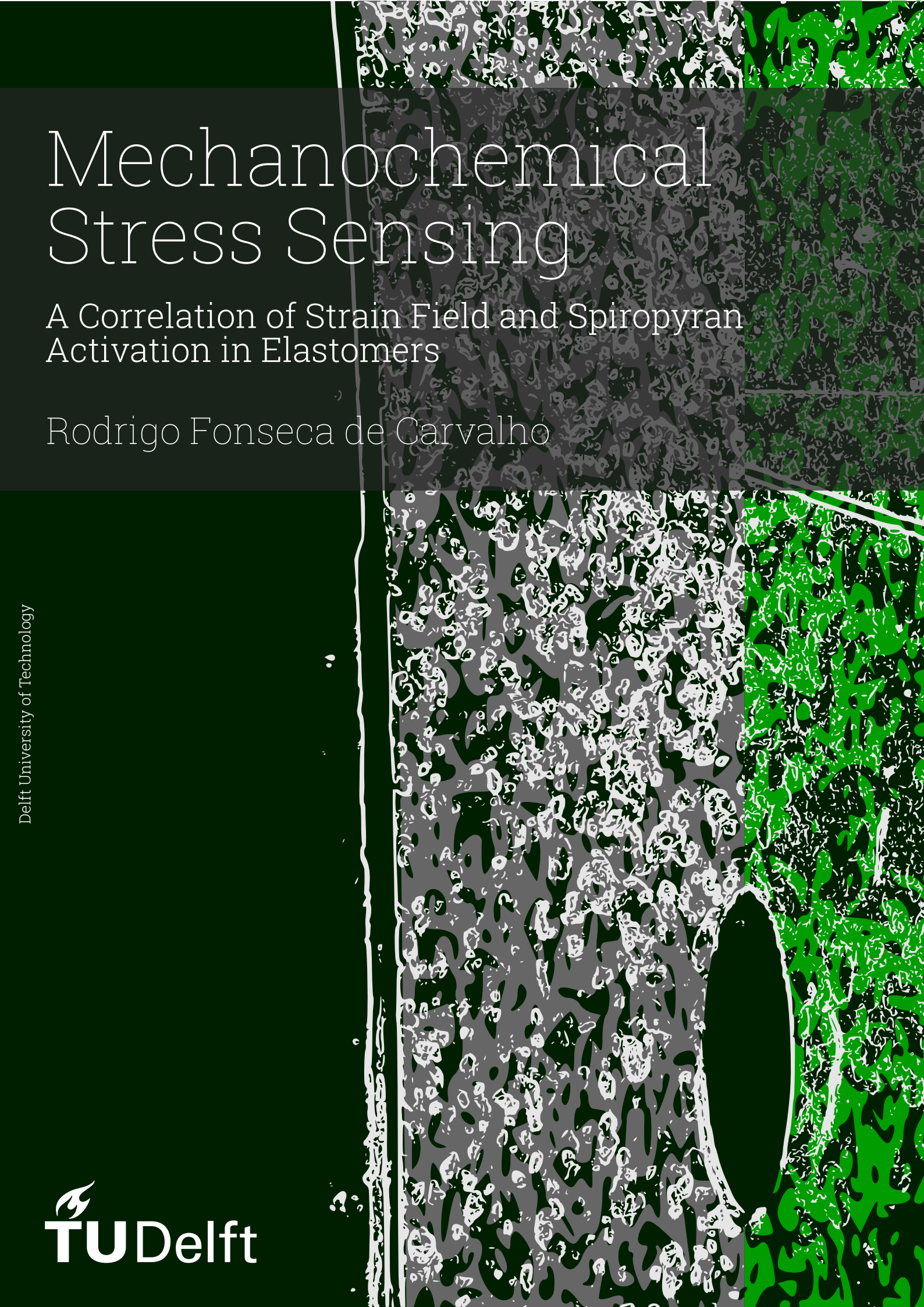

TU Delft

Mechanochemical Stress Sensing

A Correlation of Strain Field and Spiropyran Activation in Elastomers

by

Rodrigo Fonseca de Carvalho

to obtain the degree of Master of Science
at the Delft University of Technology,
to be defended publicly on Tuesday September 30, 2025 at 14:00.

Student number:	5041171	
Project duration:	January 17, 2025 - September 30, 2025	
Thesis committee:	Dr. ir. G. A. Filonenko,	TU Delft, supervisor
	Dr. S. Kumar,	TU Delft
	Dr. J. Jovanova,	TU Delft

This thesis is confidential and cannot be made public until December 31, 2025.

Cover:	Designed and created by David Plazas
Style:	TU Delft Report Style, modifications by Daan Zwaneveld

An electronic version of this thesis is available at `http://repository.tudelft.nl/`.

TU Delft

Abstract

Classical mechanochemical kinetics do not explain the persistent and history-dependent fluorescence patterns observed in spiropyran (SP) to merocyanine (MC) transitions within elastomers. This thesis addresses this gap by developing a dual-imaging methodology that integrates Digital Image Correlation (DIC) with fluorescence imaging to establish a reproducible correlation between local strain fields and mechanophore activation. The approach employs synchronized acquisition under alternating green and near-infrared illumination, enabling co-registered speckle and fluorescence images at identical mechanical states. A custom-built hardware and software was implemented, combining automated stage control, LED modulation, and image capture within a unified interface. This framework ensures temporal and spatial alignment, while allowing full-field strain analysis and fluorescence quantification across identical deformation steps. The developed methodology demonstrates that fluorescence activation systematically coincides with regions of strain localization. While low-strain sensitivity is constrained by illumination artifacts, the integrated imaging provides robust quantitative correlations at higher strains. Beyond the immediate results, the framework establishes a transferable platform for testing mechanophores as molecular stress sensors, with applications in diagnostics, materials design, and the broader study of mechanochemistry in soft matter.

Preface

As my thesis comes to an end, I find myself nostalgic for all the wonderful experiences and people that have touched my life. I would not be the person I am today without them and the lessons they have taught me. With no idea what awaits me next, I would like to take this space to reflect a bit, both on this thesis and the past few years, and to thank and acknowledge those who deserve it.

When I started this degree, I was unsure of what to expect—not in quality or content, but in what I wanted from it and what I could take from it. It felt, and was by any metric, a shot in the dark; a consequence of uncertainty. In retrospect, it was always about what I could make of it, and I was naïve to assume I had control over what it would give me. It taught me the extent of my resilience, that giving up is not my style even when I am the least qualified person in a room, and, more importantly, to hold more trust in my intuition. Throughout the last months of this thesis, the constant need for decision-making and critical thinking really proved that.

My supervisor, Georgy Filonenko, has been instrumental in getting me here, teaching me that any problem is one good idea away from being solved, and that a good conversation can yield more than months of research. Without his knowledge, expertise, and (more often than not) patience, the path to the end would have been insurmountably more complicated than it was. Thank you for taking me under your wing, and beyond a supervisor, I will always think of you as a friend.

The friends I have made through this process I will hold on to forever. My deepest thanks to Pietro, whose knowledge and kind heart were instrumental in getting this far, both in the year and the project. I want to extend my gratitude to many more people I cherish: Alexandra, Maria, David, Alison, Ishaan—your being in my life has made this academic career all the more rewarding. I would not wish to have gone through this with anyone else. Carol and Isa, my oldest friends and home far from home, you are the reason I know success and my truest inspiration. I truly love you all, and I consider myself incredibly lucky to know you.

Finally, and most importantly, to my family—my mom and dad, Eva and Mauricio—I am forever grateful for all the things you have sacrificed for me to get here, for teaching me empathy through resilience, and that if things have not gone right, it just means they have not ended yet—*Nada vai dar certo mas tudo se resolverá, eu amo vocês*. To my sister, Rafa, thank you for supporting me and bringing me down to reality when I soar too close to the sun.

I believe that covers it. Through tears of anguish, joy, sweat, and a concerning amount of caffeine, this is the final culmination of my work.

Thank you again for everything.

Rodrigo Fonseca de Carvalho
Delft, September 2025

Acronyms

BSI back-side illumination.

CMOS Complementary Metal-Oxide-Semiconductor.

DIC Digital Image Correlation.

LED Light-Emitting Diode.

MC Merocyanine.

MOSFET Metal–Oxide–Semiconductor Field-Effect Transistor.

NIR near-infrared.

PDMS polydimethylsiloxane.

SP Spiropyran.

UV Ultraviolet.

Contents

1

Introduction

Recent research demonstrates that mechanophore-embedded polymers exhibit non-classical responses under mechanical loading, where both stress history and residual strain influence chemical activation. Unlike conventional kinetic models, which primarily describe instantaneous stress–strain behavior, these materials effectively record the path of loading at the molecular level. This capability is particularly relevant for high-performance applications—such as lightweight elastomers in ballistic protection—where materials must withstand extreme deformation while simultaneously providing information about their internal mechanical state.

Mechanophores, defined as force-responsive molecules, provide a unique opportunity to address this challenge. Their activation leads to chemical transformations that can be detected optically, most often through fluorescence or colorimetric shifts. A widely studied example is the spiropyran–merocyanine (SP–MC) isomerization, which serves as a sensitive and reversible mechanochemical probe when embedded in polymeric matrices. Despite these advantages, fluorescence signals are not inherently quantitative and require calibration against independently measured strain fields to establish their reliability as indicators of stress or strain.

Digital Image Correlation (DIC) offers a complementary perspective by providing full-field, non-contact measurements of displacement and strain. Through optical tracking of surface patterns during deformation, DIC produces high-resolution strain maps that capture the continuum mechanical response of the specimen. By integrating DIC with mechanophore-based fluorescence, it becomes possible to bridge the gap between macroscopic mechanics and molecular sensing, enabling the exploration of whether optical activation can serve as a quantitative reporter of strain.

This thesis investigates the correlation between strain fields obtained via DIC and the mechano-chemical activation of spiropyran in a Polydimethylsiloxane (PDMS) matrix. The research develops a dual-imaging methodology that combines synchronized fluorescence imaging and DIC analysis under tensile loading, to evaluate whether fluorescence intensity can be quantitatively mapped to local strain distributions. For this, a custom experimental setup was designed, incorporating synchronized illumination, automated image acquisition, and controlled strain application. The results are expected to establish a foundation for quantitative stress sensing.

In order to achieve this goal, the thesis is organized into six main chapters. Chapter 2 presents a literature review of stress detection methods, with emphasis on mechanophore chemistry and DIC, establishing the theoretical foundation. Chapter 3 introduces the problem statement, research motivation, and research questions, defining the scope of the study. Chapter 4 describes the experimental methodology, including the custom-built set-up, sample preparation, and procedures for fluorescence imaging and DIC integration. Chapter 5 reports the full developed methodology, offering user guides to ensure ease of future testing as well as displaying the graphical results. Chapter 6 continues analyzing strain fields from DIC, fluorescence activation of spiropyran, and their correlation under tensile loading. Chapter 7 concludes with the main findings, addresses limitations, and outlines potential improvements for future work.

2

Literature Review

2.1. Introduction

Engineering materials are inevitably subject to degradation and failure when exposed to mechanical, thermal, or environmental loading. Understanding and mitigating such failure processes has been a longstanding objective in material science and engineering, particularly in fields where safety and reliability are critical. Traditionally, the study of failure has focused on quantifying the limits of material strength, fatigue resistance, and fracture toughness. However, as applications demand lighter, more durable, and multifunctional systems, the ability to not only predict but also detect failure in real time has become increasingly important.

The lifetime of a material is influenced by multiple factors, including intrinsic properties such as microstructure and elasticity, as well as extrinsic factors such as loading conditions, environment, and manufacturing processes. Stress plays a central role in these mechanisms, arising from external forces like repeated impact or from internal processes such as thermal contraction. While knowledge of a material's maximum stress tolerance is essential for design, the ability to detect stress accumulation, microcrack initiation, or progressive strain localization can provide an additional safeguard, extending both lifetime and reliability.

This chapter reviews the fundamental concepts of stress and its role in material failure, with emphasis on methods for detection and prevention. The discussion begins with an overview of conventional approaches to stress analysis, including analytical models, computational simulations, and experimental techniques. It then examines mechanophores as a novel chemical approach to stress detection, focusing on the spiropyran–merocyanine system as a force-responsive probe. The review further considers DIC as a complementary optical method for strain mapping, highlighting its strengths and limitations. Together, these insights establish the foundation for the hybrid mechanochemical–mechanical approach explored in this thesis.

2.2. Background: Stress considerations

2.2.1. Aspects of Stress

Stress (σ) has conceptually been known to humanity since ancient times, though it was understood in an intuitive and empirical manner. In simplified terms, stress is best defined as the force (F) applied over a cross-sectional area (A), expressed as:

$$\sigma = \frac{F}{A} \tag{2.1}$$

Stress concentrations are defined as regions experiencing stress higher than the surrounding areas, influencing the mechanical integrity and durability of materials and structures; these peaks often act as initiation points for damage and eventual failure. Depending on the scale at which it is observed stress can be characterized at different length scales.

At the macroscopic scale, the focus is on larger objects observable without the need of aides, typically millimeters to meters. At this scale, the continuum assumption is commonly used, allowing engineers to simplify materials by assuming homogeneous behavior. Stress concentrations typically occur near geometric irregularities such as holes, notches, cracks, or joints and classical elasticity theory can be used to quantify and predict stress concentration factors, thereby assisting in the identification of potential structural weaknesses and the optimization of designs to avoid failure [20].

In micromechanics, structures such as grains, fibers, inclusions, and voids influence stress distribution and localization. At this scale, inconsistencies within a material significantly alter local stress distributions, leading to stress concentrations around microstructural defects or interfaces. Nanomechanics extends analysis to atomic and molecular scales, where stress concentrations are dictated not only by geometric or microstructural irregularities but also by atomic-level defects, molecular interactions, and surface phenomena [20].

2.2.2. Types of Stress

Because of the complexity of stress, there are many ways to categorize it, each with its subsets,for simplicity, they are subdivided into two categories: external and residual stresses.

External Stresses:
These stresses result from applied loads, and the nature of the load determines how the material experiences them. From William D. Callister's *Material Science and Engineering* [20], the primary ones have been defined as:

1. **Tensile Stress:** Occurs when a material is subjected to a pulling force, causing it to elongate. It is calculated by dividing the applied force by the original cross-sectional area.
2. **Compressive Stress:** Results from a pushing force applied to a material, leading to its compression or shortening. It is calculated using the same formula as tensile stress, but the force is applied in the opposite direction.
3. **Shear Stress:** Arises when a force is applied parallel to a surface, causing one part of the material to slide relative to another.
4. **Torsional Stress:** A type of shear stress that occurs when a material is twisted, which is related to the angle of torque.

In addition to these, corrosive and thermal stresses are also considered external stresses and have a importance role in mechanical failure.

Residual Stresses:
Residual stresses can often occur without external loading and may result from factors such as heating, cooling, machining processes, or material impurities. [16]. Within the world of metals these can develop through plastic deformation (e.g., machining and grinding), non-uniform cooling (e.g., welding and casting), or cooling-induced phase transformations, which can cause changes in density, potentially resulting in warping or distortion [20].

Within polymers, the reaction to increasing internal stresses can vary significantly, as can their properties. Since polymers are typically machined or formed through molding and curing, these processes can induce residual stresses. The large range of expansion coefficients and cure shrinkage in these materials can lead to residual stresses at the microscale, and the addition of fiber or additives can result in compressive stresses [42]. Alternatively, some polymers are classified as hyper-elastic and exhibit a non-linear elastic response, minimizing permanent residual stress accumulation, a topic further discussed in the following section [34].

Constitutive Modeling of Stress

Constitutive modeling refers to the description of mechanical properties using mathematical formulations grounded in experimental research, which represents a key component in mechanics and forms the basis of stress determination. The concepts presented here are based on the work of Ristinmaa and Ottosen [34]. In the context of polymers, constitutive modeling is essential due to their complex mechanical behavior, which often includes combinations of elastic, plastic, viscoelastic, non-linear, and hyperelastic responses.

For small deformations and small strain rates, many solids are approximated as linearly elastic. This relies on continuum mechanics and, specifically, Hooke's law as shown in equation 2.2. The stress tensor is linearly related to the strain tensor, also known as Cauchy-elasticity. Polymers,however, tend to exhibit nonlinear behavior, becoming brittle at low temperatures and exhibiting increased viscosity above the glass transition, known as viscoelasticity [20]. Such modeling is essential for accurately capturing the stress-strain response of soft, rubber-like polymers, which recover their original shape but exhibit pronounced nonlinearity in deformation.

$$\sigma = E * \epsilon \tag{2.2}$$

For larger deformations, typical in elastomers and soft polymers, hyper-elastic models are utilized, developed through the fundamental relations of strain energy density function with respect to the strain tensor, as seen in equation 2.3. This model states that "Elastic response is independent of the load history" [34], such that the material is not affected by residual stresses and further implies both mechanical and thermodynamic reversibility.

$$\sigma_{ij} = \frac{\partial W}{\partial \varepsilon_{ij}} \tag{2.3}$$

Lastly, the transition between loading and unloading is defined by 'Plasticity Theory', which determines if the yielding of a material has begun. This mathematically distinguishes the elastic and plastic regions of strain into reversible (ε^e_{ij}) and irreversible (ε^e_{ij}), respectively, shown in equation 2.4. For general stress states, the failure or initial yield criteria are determined by the plastic stress which, for homogeneous materials, is defined by functions that describe their behavior.

$$\varepsilon_{ij} = \varepsilon^e_{ij} + \varepsilon^p_{ij} \tag{2.4}$$

von Mises Criterion:
This criterion is the most widely used initial yield model for isotropic ductile materials under uniaxial stress application. Assuming that yielding is independent of the hydrostatic stress and is governed entirely by the invariant of the deviatoric stress tensor (J_2), the criterion is given by the relation:

$$F(J_2) = \sqrt{3J_2} - \sigma_{y0} = 0 \tag{2.5}$$

Drucker–Prager Criterion:
The Drucker–Prager criterion is a yield condition designed to model pressure-sensitive materials such as rocks, concrete, and certain polymers. Unlike the von Mises criterion, which is based solely on shear stress, the Drucker–Prager model includes the influence of hydrostatic (mean) stress, making it more suitable for materials that yield differently under tension and compression. In Equation 2.6, J_2 is the second invariant of the deviatoric stress tensor, I_1 is the first invariant of the stress tensor, and α and β are material parameters representing pressure sensitivity and yield stress, respectively.

$$\sqrt{J_2} + \alpha I_1 = \beta \tag{2.6}$$

Tresca Criterion:
Also known as the maximum shear criterion is one of the earliest and simplest yield models, useful for modeling ductile materials under multi-axial stress states. Tresca assumes that Plastic deformation occurs when the maximum shear stress reaches a critical value equal to uniaxial tension. This parameter is given by equation 2.7, where σ_1, σ_2, and σ_3 are principal stresses, while σ_{y0} is the uniaxial yield stress in tension. It should be noted that this equation ensures a yield that begins when the maximum shear stress reaches $\tau_{\text{max}} = \frac{\sigma_{y0}}{2}$.

$$\max\left(|\sigma_1 - \sigma_2|,\ |\sigma_2 - \sigma_3|,\ |\sigma_3 - \sigma_1|\right) = \sigma_{y0} \tag{2.7}$$

Mohr–Coulomb Criterion:
The Mohr-Coulomb yield criterion is a classical failure model used to describe the shear strength of frictional materials, such as concrete, rocks and some types of polymers. It is based on the assumption

that the value of the shear stress on a plane is linearly proportional to the normal stress on the plane. Commonly used for brittle failure [2], equation 2.8 presents the general form, where τ is the shear stress on the failure plane, σ is the normal stress on the failure plane, c is the cohesion (i.e., the shear strength when $\sigma = 0$), μ is the coefficient of internal friction, and ϕ is the angle of internal friction. This can also be given as equation 2.9 in the principal stress state.

$$\tau = c + \sigma \tan \phi \tag{2.8}$$

$$\sigma_1 - \sigma_3 = \frac{2c \cos \phi}{1 - \sin \phi} + \frac{1 + \sin \phi}{1 - \sin \phi} \sigma_3 \tag{2.9}$$

2.3. Failure Mechanisms and Detection

A critical aspect in understanding a material's behavior is understanding the failure mechanics that are dominant for its structure, which can be dependent on many material properties and scale. While intrinsically related at smaller scales, a more complex explanation of fracture and failure mechanisms can be developed.. At the macroscale, the material behaves uniformly and the stress and yielding points are defined by overall properties. At the microscopic scale, the material's internal structure consists of grains, formed by sequences of atoms in crystalline arrangements. At this scale, slipping between atomic planes is a common failure mode, where blocks of crystals are displaced along specific crystallographic directions. In polycrystalline materials, multiple slip systems activate, resulting in homogeneous plastic deformation at the macroscale [18]. This assumption is valid when deformation can be described using continuum mechanics [20].

At smaller scales these deformations accumulate, and while a single micro-fracture is not sufficient to cause failure, but the accumulation of several micro-fractures can lead to overall failure. In polymers this occurs through bond scission, while in metals and other less ductile materials through fracturing [14].

2.3.1. Stress Mapping Techniques

The need to accurately track stress distribution has led to the development of various techniques such as computational, analytical, and experimental. These approaches differ in the form of processing and the assumptions taken. In practice, these techniques are often used in combination with the others to ensure a reliable result.

Analytical Techniques

This approach involves quantifying stress and strain using mathematical equations and mechanical models, typically involving closed-form solutions based on equilibrium, compatibility, and constitutive laws. For example, under the continuum assumption, applying a uniform load until failure allows for straightforward measurement of true stress and strain. These approaches commonly incorporate the deformation criteria and can generally be summarized as follows [21]:

- **Classical Elasticity Solution:** This method solves equilibrium equations with boundary conditions to estimate stress/strain in beams, plates, and shells.
- **Thermal Stress Models:** Formulations such as $\epsilon_t = \alpha \Delta T$ are used to estimate thermal strain/stress in constrained and unconstrained bodies
- **Tensile Test Interpretation:** Experimental in execution, it provides essential input for analytical modeling (e.g., Young's modulus, yield strength)

Computational Techniques

Computational approaches utilize numerical and simulation methods to predict the stress and strain of a material across a 2-dimensional area. The most common example of this is Finite Element Analysis(FEA), which utilizes a mesh separation, where the area is divided into multiple elements, connected through nodes. By tracking the nodes throughout the deformation it is capable of creating a stress map. Some methods for this include the Finite Element Method, Finite Volume Method, and the Finite Difference Method.

DIC follows a similar principle: it uses a random speckle pattern to track displacement during deformation and generate stress maps. Often, DIC is used to validate other computational and experimental methods. For all computational techniques some experimental data is needed, thus this is often accompanied by forms of destructive sample deformation, such as tensile testing or thermal imaging.

2.4. Background: Mechanics of Mechanophores

2.4.1. Mechanophores (MP)

When considering novel approaches to stress detection, MPs are a widely discussed topic; they are a class of stimuli-responsive materials used for stress sensing. MPs are specialized, mechanically responsive molecules designed to exhibit a visual indication upon application of mechanical force. This offers a chemistry-based stress mapping technique known as 'Mechanosensing', although other stimuli can cause the same reaction, as seen in Figure 2.1. This visual indication is typically a change in color (mechanochromic response) or fluorescence activation (mechanoluminescence) of the material, which can help identifying subcritical stress concentrations in bulk materials, potentially providing insights into microfractures or crazing prior to failure [12].

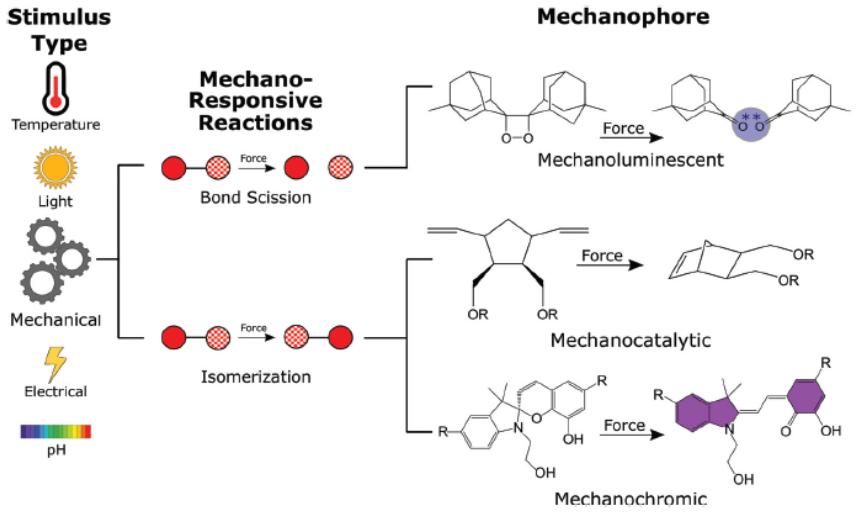

Figure 2.1: Mechanophores and their stimulus types [12]

Typically, mechanosensing molecules are embedded within polymer matrices and are covalently attached, such that when the material is deformed the molecule undergoes a chemical reaction. This technique is capable of stress mapping in the material through all scales, as the resolution of the phenomenon is limited only by the wavelength of the light. This chapter will focus on developing the mechanical and chemical theory behind the mechanosensitive molecules.

By incorporating these mechanophores within a material system a real-time stress distribution can be attained. Since their discovery, many mechanophores have been identified including Diarylbibenzofuran (DABBF), Cyclobutane [41], Diels–Alder Adducts [9], and Spiropyran [17], among others. The latter will be the focus of this section, elaborating on the general mechanical and optical properties of spiropyran and detailing its specific chemistry and chemical reaction.

2.4.2. Mechano-chemistry of Spiropyran

SPs are a versatile family of photochromic molecules characterized by their ability to reversibly switch between a closed SP form (colorless) and an open MC form (intensely colored) upon exposure to different external stimuli. These include Ultra-Violet (UV) light, temperature, pH, and electric fields. The molecular switch involves the cleavage of the spiro-carbon-oxygen bond, transforming a closed SP into an open MC form, as seen in Figure 2.2. This transition involves significant structural and electronic rearrangements, typically from a neutral, closed-ring SP to a planar MC form [23].

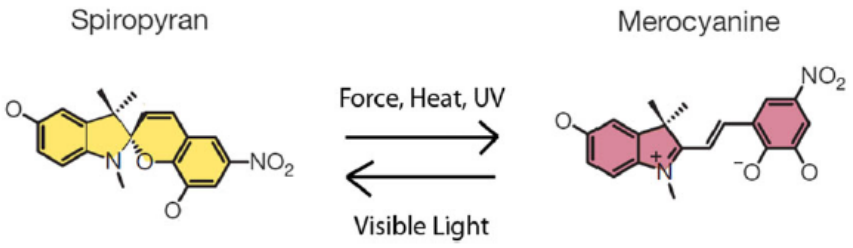

Figure 2.2: Scission of C-O bond; Spiropyran to Merocyanine reaction (adapted [8])

Concept: Potential Energy Surface

The concept of a potential energy barrier is central to chemical kinetics, as it defines the energy threshold that reacting molecules must overcome to transition from reactants to products. In classical terms, this barrier corresponds to the activation energy (E_a), which is the minimum energy required for a chemical transformation to proceed. This energy barrier results from the need to reach a high-energy transition state, as described by Transition State Theory (TST), where molecules undergo structural reorganization. The reaction rate is directly influenced by this barrier, following the Arrhenius equation, which shows an exponential dependence of the rate constant on the inverse of absolute temperature and the activation energy:

$$k = A \exp\left(-\frac{E_a}{RT}\right) \tag{2.10}$$

Where k is the rate constant, A the pre-exponential factor, R the gas constant, and T the absolute temperature. This relation underscores the strong sensitivity of reaction rates to thermal energy, wherein even small increases in T can substantially increase the proportion of molecules capable of surmounting the potential barrier [10].

However, in reversible or multi-step reactions, the net reaction rate in such systems is not a simple function of a single barrier, but rather the result of competing forward and reverse pathways, each characterized by distinct transition states and rate-controlling steps. Here, reversibility is not simply a thermodynamic condition ($\Delta G \approx 0$) but also a kinetic property that depends on the ability of molecular species to surmount their respective energy barriers in both directions [10], as described by the De Donder equality.

$$\frac{r^+}{r^-} = \exp\left(-\frac{\Delta G}{RT}\right) \tag{2.11}$$

Even at equilibrium (where net rate = 0), both forward and reverse reactions may be kinetically active, traversing distinct transition states. Thus, reversibility is dynamically maintained (Fig. 2.3), not statically imposed. Importantly, it is emphasize that kinetic reversibility requires the presence of viable microscopic pathways in both directions, with sufficient population of reactants and intermediates, and appropriate activation energies [28].

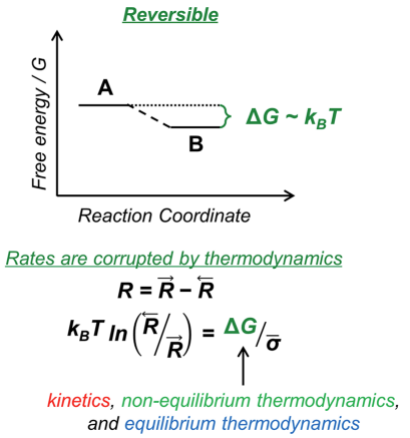

Figure 2.3: Effect of proximity to equilibrium on chemical reaction rate and direction. Net rate (R), forward rate ($R_{\rightarrow}$), reverse rate ($R_{\leftarrow}$), Gibbs free energy (G), and average stoichiometric coefficient ($\bar{\sigma}$)[28]

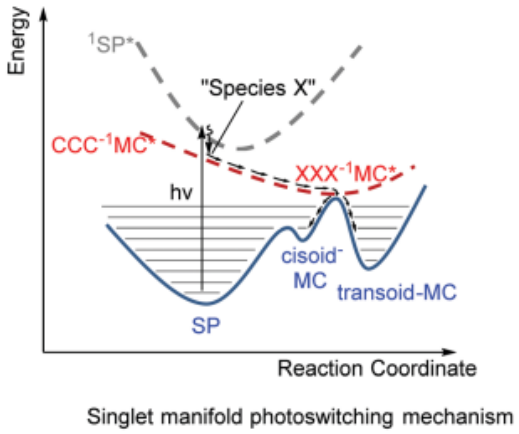

Figure 2.4: Photochemical ring opening energy barrier [43]

Activation Requirements and Reversibility:
The activation of SP to its open-ring MC form is governed by a combination of structural, energetic, and environmental factors. This transformation involves cleavage of the spiro C–O bond and requires overcoming a potential energy barrier, which can be modulated by external stimuli such as mechanical force, light, or solvent polarity. This section elaborates on the leading concepts behind its mechano- and photo-sensitivity.

Photo-activation:
For the activation via exposure to UV light, the photon absorption pushes the molecule from a ground state (S_o) to an excited state (S_{1or2}). Based on the work of Zhai et al. [43] the required photon energy for excitation is typically 3.5–$4.0\,\mathrm{eV}$, corresponding to a wavelength of approximately 312–$350\,\mathrm{nm}$.

Upon excitation, relaxation proceeds along a pathway where the C_{spiro}-O bond stretches as a consequence of nuclear motion. Importantly, no significant energetic barrier remains after excitation. Once the system becomes excited the reaction becomes nearly barrierless and progresses to bond rupture within 0.6–$1.0\,\mathrm{ps}$. [43].

To further explain this concept, the figure 2.4 is provided [43]. Following excitation, nuclear motion, the bond stretching around C_{spiro}-O and twisting surrounding bonds, lead the system toward a conical intersection (a point where the excited and grounded states come very close in energy). Through this intersection, the molecule undergoes radiationless relaxation back to the ground state surface, resulting in bond cleavage and the formation of the open MC structure [23].

Mechanochemical activation:
Mechanochemistry refers to the study of mechanically driven chemical reactions, typically within a polymer, which when stretched into non-equilibrium geometries significantly alters their reactivity. At a macroscopic scale, the homogeneous elongation of the material is, to some extent, proportional to the stretching of the microscopic single chain; some of which stretch far enough to induce chemical reactions. Even modest forces ($\approx 5\,\mathrm{nN}$) applied to polymer chains such as polystyrene can lower bond lifetimes from geological timescales to milliseconds at room temperature [40].

The mechanochromism of spiropyran requires an environment that stabilizes the MC, so it is often embedded into the matrix of polymeric structures. When this happens, an induced change in the molecule can result in ring opening reactions to reduce the stress experienced [23]. Therefore, three forms of mechano-sensitive SPs have been identified and studied, as shown in Fig. 2.5, labeled SP1, SP2 and SP3. The first two are both UV and mechanically activated while SP3 is only mechanically activated [40].

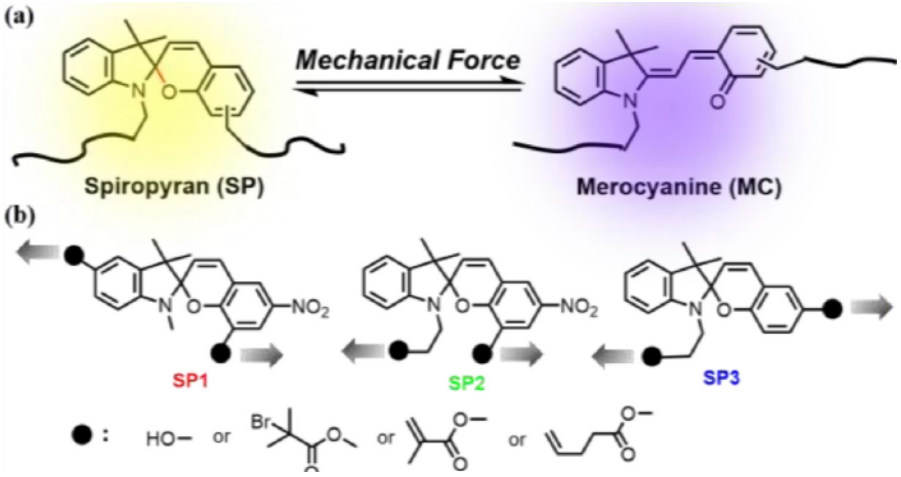

Figure 2.5: Force-induced Spiropyran to Merocyanine reaction showing load bearing attachment [25]

Considering the kinetics of this reaction, in the absence of external forces, a substantial activation barrier (≈120–140 kJ/mol or approximately 1.24–1.45 eV) must be overcome thermally or via electronic excitation to break the C_{spiro}-O bond, converting the closed SP structure into the open MC form. Under an applied mechanical load (approximately 1.5–2.0 nN), this activation barrier is significantly lowered or entirely eliminated due to mechanical work performed directly along the molecular reaction coordinate. Consequently, the MC state becomes energetically accessible at ambient conditions without thermal or photochemical input [1].

2.4.3. Stress Mapping with Mechanophores

Through the use of modern material science applications, SP has been utilized as an accurate method of stress mapping, promoted by the increased mechanosensitivity when embedded in a polymer matrix. This section summarizes recent research and uses of these mechanophores.

Quantifying Localized Stresses in the Matrix of a Fiber-Reinforced Composite via Mechanophores [15]

This study aims to quantify the localized stresses in the matrix of a fiber-reinforced composite undergoing a force induced transformation, where SP converts to the fluorescent MC. In this study, Haque utilized PDMS samples with 0.6 wt% concentration of SP subjected to uniaxial loading while the mechanophore activation was monitored using confocal microscopy. To avoid influence from geometrical changes, a rigid glass sphere was placed within the sample; the fluorescence was then quantitatively interpreted into stress using the numerical analysis technique FEA.

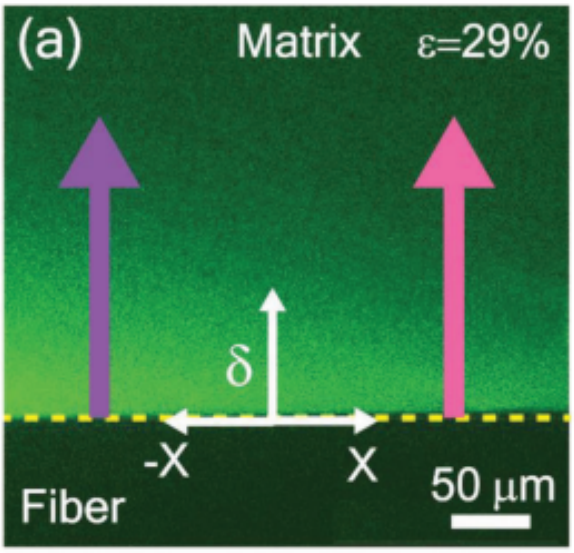

Figure 2.6: Gradient of MP activation intensity decreasing into the matrix [15]

The author found that high-intensity fluorescence was observed near the fiber-matrix interface, indicating stress localization in that region, additionally, a visible stress gradient was identified decreasing with distance from the fiber shown in Figure 2.6. The stress range in the matrix was quantified to be between 1.2 and 2.5 MPa, derived by applying the established calibration (0.26 MPa^{-1}) to fluorescence intensity maps.

This method validates mechanophores as quantitative stress tensor in composite systems, an approach that allows high resolution three dimensional visualization of the internal stresses. This demonstrates a direct correlation between the fluorescence and stress concentration without the need for external markers or assumptions.

Mechanochemistry of Spiropyran under Internal Stresses of a Glassy Polymer [17]
This study investigates the internal residual stresses formed during polymer vitrification under no external mechanical loading. These stresses can alter the isomerization kinetics between the SP and the fluorescent MC form, with measurable shifts in the activation energy. The isomerization rate of SP $\rightarrow$ MC in Polymethyl Methacrylate (PMMA) matrices was analyzed under different thermal and topological conditions; changes in activation energy (up to $\sim$70 $\frac{kJ}{mol}$) were used as indirect indicators of internal stress.

To perform the tracking and imaging, the SP $\rightarrow$ MC reconversion was monitored via the decay in photoluminescence. The fluorescence lifetime was mapped across the samples using confocal imaging, correlating with the local stresses as shorter lifetimes equate to higher compressive stresses. The authors concluded that internal compressive stresses lowered the activation energy for MC $\rightarrow$ SP, contrary to what was expected, while inhibiting the reverse reaction.

Strain and stress mapping by mechanochemical activation of spiropyran in PMMA [8]
Celestine et al. (2019) employed spiropyran crosslinked into a rubber-toughened PMMA matrix, at a concentration of 0.005 mol%, to visualize and quantify stress and strain fields ahead of a propagating crack. By coupling fluorescence imaging with DIC and analytical stress field solutions,Hutchinson–Rice–Rosengren (HRR) singularity fields, they demonstrated that SP activation provides both qualitative and quantitative insights into the mechanical field surrounding a crack tip.

The experimental set-up was such that a single edge notch tension specimen was tested under uniaxial loading. The DIC developed the strain field and was converted to equivalent strain utilizing the HRR field equation 2.12, based on fracture mechanics and constitutive parameters, the stress field was determined. The resulting plots can be seen in Figure 2.7.

$$\sigma_{ij} = \sigma_Y \left[\frac{J}{\alpha \sigma_Y \varepsilon_Y I_n r} \right]^{\frac{1}{n+1}} \hat{\sigma}_{ij}(\theta, n) \tag{2.12}$$

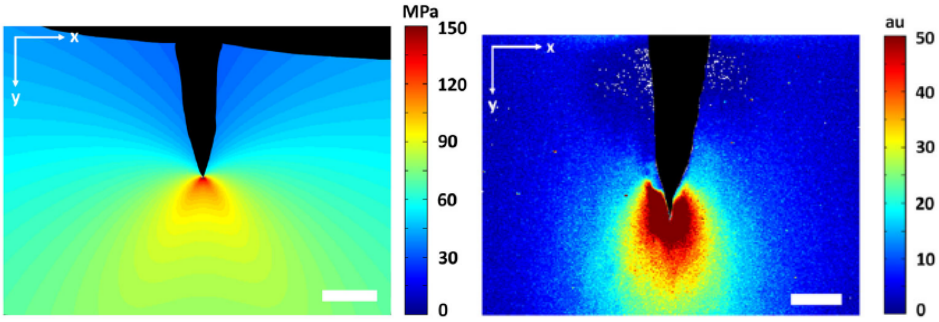

(a) Equivalent stress spatial plot **(b)** Intensity spatial plot

Figure 2.7: Stress and intensity plots utilizing DIC from [8] at Δa = 0.4 mm (scale bar: 0.5 mm)

Fluorescence intensity showed a power-law decay with distance from the crack tip, with a decay exponent ($\beta \simeq 1.42$) steeper than that of equivalent strain ($\beta \simeq 0.69$) or equivalent stress ($\beta \simeq 0.15$). The authors defined an activation strain ($\simeq$3.8–5.2%) and activation stress ($\simeq$69–72 MPa) as the threshold for SP isomerization, allowing for an estimation of local stress and strain in samples lacking direct mechanical measurements. These results demonstrate that spiropyran mechanophores can be calibrated as molecular stress sensors for fracture analysis and damage detection.

Summary: Novel approaches to mechanophores

The reviewed studies demonstrate varied strategies for utilizing SP-based mechanophores to map stress fields in polymer systems. Haque [15] developed a method to quantify local stress in fiber-reinforced composites by embedding SP in PDMS and correlating fluorescence intensity with finite element simulations. This allowed for the visualization of stress gradients around rigid inclusions under uniaxial loading. In contrast, Janissen and Filonenko (2022) [17] investigated internal residual stresses formed during polymer vitrification in PMMA, using fluorescence lifetime mapping to detect stress-induced shifts in isomerization kinetics without applying external forces.

Celestine et al. (2019) [8] combined mechanophore activation with digital image correlation and HRR field theory to analyze the mechanical field ahead of a propagating crack in a rubber-toughened PMMA matrix. By aligning fluorescence intensity with strain and stress fields derived from fracture mechanics, they defined threshold activation conditions for SP. Collectively, these studies establish mechanophores as adaptable tools for stress detection across diverse conditions, including externally applied, residual, and fracture-induced stresses.

2.5. Approach: Digital Image Correlation (DIC)

DIC is a full-field optical metrology technique designed to measure displacement and strain on object surfaces, operating across length scales from macro to nano. As a method, DIC has matured from its initial implementations in the early 1980s using coarse-resolution analog imaging to today's high-resolution, multi-dimensional, and multi-physics applications, including strain mapping, fracture mechanics, biomechanics, and damage prediction. This evolution is grounded in a robust theoretical framework that links image intensity patterns to material deformation kinematics and mechanical stress states.

2.5.1. Theory

At its foundation, DIC assumes that the surface of a material contains a unique, randomly distributed pattern, the speckle field, whose spatial intensity distribution remains consistent during deformation, merely translating and distorting along with the underlying material points. If we denote the grayscale intensity of a point $x = (x, y)$ in the reference (undeformed) image as $f(x)$, and in the deformed image as $g(x')$, the goal of DIC is to find the transformation $x \mapsto x' = x + u(x)$ that best aligns the two, under the assumption shown in equation 2.13 [4].

$$f(x) \approx g(x + u(x)) \tag{2.13}$$

For small subsets centered around a point X_o, the displacement field u is often approximated using a first-order Taylor expansion, as shown in Equation 2.14 [6, 37], which uses the deformation gradient tensor. This affine model captures translations, rotations, and in-plane strain components, and enables pixel-wise calculation of displacement fields through optimization of correlation functions. The correlation function is typically used is the normalized cross-correlation or sum of squared differences. Its optimization is done either by exhaustive search or gradient-based techniques like the Newton-Raphson method [6], which enables subpixel resolution in displacement estimation [8].

$$u(x + \mathrm{d}x, y + \mathrm{d}y) \approx u(x, y) + \frac{\partial u}{\partial x}\,\mathrm{d}x + \frac{\partial u}{\partial y}\,\mathrm{d}y \tag{2.14}$$

Once the displacement field $u(x, y)$ is known, the strain field is computed by differentiating the displacement gradients. For small deformations, the linear strain tensor is:

$$\varepsilon_{ij} = \frac{1}{2}\left(\frac{\partial u_i}{\partial x_j} + \frac{\partial u_j}{\partial x_i}\right) \tag{2.15}$$

In practice, this process is sensitive to noise, particularly when displacement fields are obtained from discrete image data. The accuracy of strain computation is fundamentally linked to the subset size, speckle pattern quality, and interpolation scheme used (e.g., bicubic splines). Berfield et al., demonstrated that with careful calibration and airbrush-based speckle generation, displacements down to $1\,\mathrm{nm}$ at the microscale and $17\,\mathrm{nm}$ at the nanoscale could be resolved [3].

DIC itself does not measure stress — it infers displacement and strain. To derive stress fields, DIC results must be coupled with material constitutive models. In linear elasticity, the generalized Hooke's law links the stress tensor σ_{ij} to the strain tensor ϵ_{kl}, where C_{ijkl} is the fourth-order elasticity tensor as seen in Equation (2.16). For isotropic materials under plane stress or plane strain assumptions, this simplifies to formulations involving only Young's modulus E and Poisson's ratio ν.

$$\sigma_{ij} = C_{ijkl}\,\varepsilon_{kl} \tag{2.16}$$

2.5.2. Sample Considerations

Having discussed the mathematical basis for DIC, the practical accuracy and success of any DIC experiment depend critically on how the sample is prepared and how the speckle pattern is generated. These elements determine not only the reliability of the displacement field but also the measurable deformation and the correlation process.

The ideal specimen for DIC is optically accessible, geometrically stable, and provides sufficient surface or internal optical contrast for imaging. For surface DIC, matte finishes are preferred to avoid glare

or specular reflection, which corrupt grayscale data. Transparent or semi-transparent polymers like PDMS are particularly useful for internal DIC applications, allowing speckle layers to be embedded within the bulk material and imaged using transmitted or fluorescent light microscopy [3].

Speckle pattern formation is a critical determinant of accuracy in DIC. Patterns need to have good contrast, a random spatial distribution, and appropriately sized speckles, ideally around 3 to 5 pixels in diameter. These features help ensure that each correlation subset contains enough distinct intensity variation for accurate tracking. Speckle size and density are affected by parameters like spray time, nozzle diameter, and paint concentration. Patterns with smooth, continuous histograms generally perform better in terms of subpixel resolution and stability [13]. Excessively large or dense speckles reduce correlation accuracy by limiting local intensity variation, while low-density patterns may lack sufficient texture [3].

As a result, DIC is inherently scale-free, provided the imaging resolution and speckle characteristics are appropriate. At the macroscale, standard spray-paint speckle patterns suffice. At the microscale, high-quality airbrushes (e.g., Iwata Micron) enable finer patterns. At the nanoscale, Berfield et al. introduced the use of fluorescent silica nanoparticles, deposited via spin coating, which fluoresce under microscope illumination and generate high-contrast speckle fields.

2.5.3. DIC: Theoretical Set-up

DIC has become a cornerstone technique in experimental mechanics due to its non-contact nature, high spatial resolution, and ability to provide full-field displacement and strain measurements. However, the quality and reliability of DIC data hinge on the experimental setup. Each component, from hardware to environmental control, plays a pivotal role in ensuring sub-pixel accuracy and measurement fidelity. This section outlines the most influential experimental parameters, highlighting their significance and defining the ideal configurations for high-quality DIC implementation.

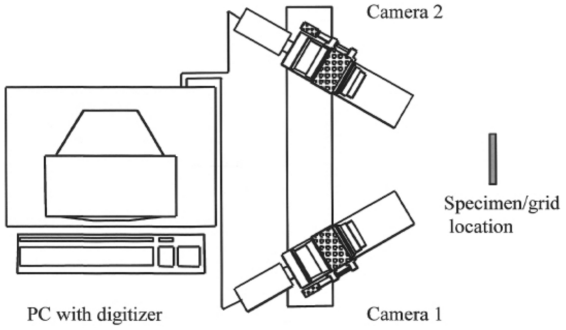

Figure 2.8: Schematic of a complete 3-D DIC set-up [37]

Stereo-Rig Configuration

In two-dimensional DIC (2D-DIC), a single camera captures in-plane surface deformations on flat specimens. This approach is simpler and less computationally demanding but is sensitive to out-of-plane motions, which can introduce significant errors. Therefore, it is best suited for planar samples undergoing pure in-plane loading, where camera alignment perpendicular to the specimen surface is critical [30]. Whether using a single or stereo setup, mechanical rigidity of the rig is paramount to preserving alignment throughout the experiment and ensuring consistent, artifact-free data.

In a three-Dimensional DIC (3D-DIC) system, a stereo-rig is used, where a dual-camera arrangement enables triangulation-based surface measurement (Figure 2.8). Its importance stems from the need for precise geometric calibration and consistent camera alignment throughout the experiment. Even microscopic shifts between cameras can introduce significant errors in displacement calculations. Therefore, the ideal stereo-rig must be rigidly constructed using a stable, low-vibration frame or optical rail system. Cameras should be firmly mounted using precision brackets or dovetail mounts to prevent any relative motion. For accurate triangulation, a stereo angle between 15° and 35° is recommended, striking a

balance between in-plane and out-of-plane resolution [37, 36, 33].

Camera and Lens Selection

Imaging sensors are critical components in a DIC system, capturing fine spatial details that later translate into meaningful mechanical insights. The significance of camera performance lies in its direct influence on spatial resolution, noise floor, and dynamic range. For optimal results, scientific-grade Complementary Metal-Oxide-Semiconductor (CMOS) cameras with high pixel density (e.g., 2 MP or higher) and bit depths of 10–12 bits are preferred. Synchronization is crucial in stereo setups to ensure simultaneous image acquisition; thus, cameras should support hardware triggering or use interfaces like CoaXPress or FireWire that offer built-in synchronization [29, 36]). Matched sensor characteristics and synchronized shutters help eliminate timing discrepancies that could otherwise distort the deformation field.

Lens choice determines magnification, field-of-view (FOV), and the clarity of the speckle pattern. Prime lenses are preferred for their low optical distortion compared to zoom lenses [37]. The focal length must be selected to balance spatial resolution and working distance—longer focal lengths improve resolution and minimize the effects of perspective changes, which is particularly important in 2D-DIC to reduce sensitivity to out-of-plane motion [39]. Lenses should be stopped down (e.g., to f/11 or f/16) to enhance depth-of-field. To avoid empty magnification, the resolving power of the lens must match or exceed the Nyquist frequency of the camera sensor [30].

Subset Size, Step Size, and Calibration

Subset size and step size are essential numerical parameters for the DIC algorithm. Subsets must be large enough to include multiple unique speckles—typically 15×15 to 29×29 pixels—to ensure accurate correlation. The step size, which controls the grid spacing of computed points, is usually set to half the subset size to balance spatial resolution and computation cost [39, 30]. Calibration, especially for StereoDIC, is critical and involves solving for both intrinsic and extrinsic camera parameters. Using high-quality grid targets and capturing images from multiple orientations enables self-calibration routines to converge with high accuracy [37, 38].

Lighting and Illumination

High-quality lighting is foundational to achieving good DIC results. The speckle pattern must be imaged with high contrast and minimal noise, both of which are largely governed by the illumination setup. Ideal lighting is flat, uniform, and diffuse—ensuring that highlights and shadows are eliminated. Matte paints should be used on specimen surfaces to avoid reflections, and light should be delivered via LED sources, which provide high intensity with minimal heat. Otherwise, heat waves or air convection patterns mimic deformation, displacing data. Additionally, direct laser illumination is discouraged due to the formation of coherent speckle patterns that mask the surface texture [32]. For this reason, halogen or incandescent sources should be avoided, and fans can be used to disrupt thermal gradients if necessary. A contrast of at least 50 gray levels (on an 8-bit scale) between light and dark speckles is recommended to optimize subset matching [31].

2.6. Literature Conclusions

This review has examined the theoretical basis for using mechanophores, particularly SP, as a method of stress detection in polymeric systems. SP undergoes a force- or light-induced isomerization to its MC form, accompanied by a measurable change in optical properties. The activation mechanism is governed by the cleavage of the $C_{spiro} - O$ bond, which is influenced by the applied mechanical energy or photon input. The underlying energy landscape, described by the potential energy surface and characterized by a reaction barrier of approximately 120–140 $\frac{kJ}{mol}$, forms the foundation for understanding the activation and reversibility of this reaction. These properties position mechanophores as viable candidates for mapping local stress concentrations in soft materials, with the potential to report mechanical events below macroscopic failure thresholds.

Recent literature has demonstrated that SP-containing systems can respond to both externally applied and internally generated stresses. Studies by Haque[15], Janissen [17], and Celestine [8] illustrate how SP mechanophores enable spatially resolved, quantitative stress detection—either via fluorescence intensity or photoluminescence lifetime—providing valuable information on local stress states in

composite matrices and glassy polymers. However, the reproducibility, calibration, and interpretation of these optical signals remain active areas of investigation, and further work is required to generalize their applicability across different polymer systems and loading conditions.

DIC is proposed as a complementary method for characterizing strain distributions within the same samples. DIC is a full-field optical technique capable of capturing in-plane displacements and deriving strain fields through image correlation. The method relies on correlating speckle patterns before and after deformation to resolve displacement and strain fields. Critical considerations in DIC implementation include speckle pattern quality (e.g., contrast, dot size, randomness), subset and step size optimization, camera resolution, lighting conditions, and system calibration. The speckle pattern must have well-defined grayscale intensity variation, with speckles typically 3–5 pixels in diameter, while system components—such as stereo-camera alignment, lens resolution, and light uniformity—must be precisely configured. Accurate DIC implementation allows coupling of mechanical strain data with mechanophore activation, supporting a hybrid imaging approach.

The combination of SP mechanophore activation with DIC presents a potential framework for correlating molecular-scale optical responses with continuum-level mechanical deformation. This approach may enable investigations into whether photoluminescent activation can be quantitatively related to local strain or stress distributions. While the theoretical alignment between these techniques is promising, their integration requires further validation. The considerations outlined in this review suggest a direction for future experimental work, which will inform the development of a problem statement and define the scope of application.

3

Thesis Plan

3.1. Problem Statement and Motivation

The mechanochemical isomerization of SP to MC is a well-established process triggered by mechanical strain or UV-irradiation. The degree of activation has been shown to scale with the energy applied to the system, causing regions under higher UV intensity or strain to show higher merocyanine concentrations. While this behavior has been demonstrated [8, 15], further quantitative validation is required.

According to classic kinetics theory, the rate of a reaction such as the MC to SP ring closure, is governed by the Arrhenius equation 2.10, as explained. Therefore, when the sample is relaxed the reverse reaction takes place, slowly returning SP to MC; in areas of residual stress, however, this reverse reaction is slower or does not occur at all [17].

Current research: Manuscript by Georgy Filonenko and Sid Kummar [24]

Recent work by Filonenko and Kumar explored this phenomenon using PDMS as a matrix for spiropyran, the hyperelastic behavior of this matherial removes the effects of residual mechanical stress as a variable. The experiments involved stretching rectangular PDMS samples (with a central hole) to 100% strain and then relaxing. The geometry of the sample was chosen for its predictable stress distribution, and the procedure employed is depicted in Figure 3.1(A), using equipment previously validated in the work by Joshi[19].

Despite the absence of residual stress, a clear and stable fluorescence pattern corresponding to SP activation was observed at strains above 0.5, aligning with reported activation thresholds, as shown in Figure 3.1(B). The intensity and distribution of these patterns matched analytical predictions, yet persisted even after complete sample relaxation. Notably, these patterns were visible under non-polarized light and under polarized light aligned with the tension direction, but not when polarized across it. The fluorescence distribution remained stable, suggesting a shift in the local chemical equilibrium that classical kinetic models do not predict.

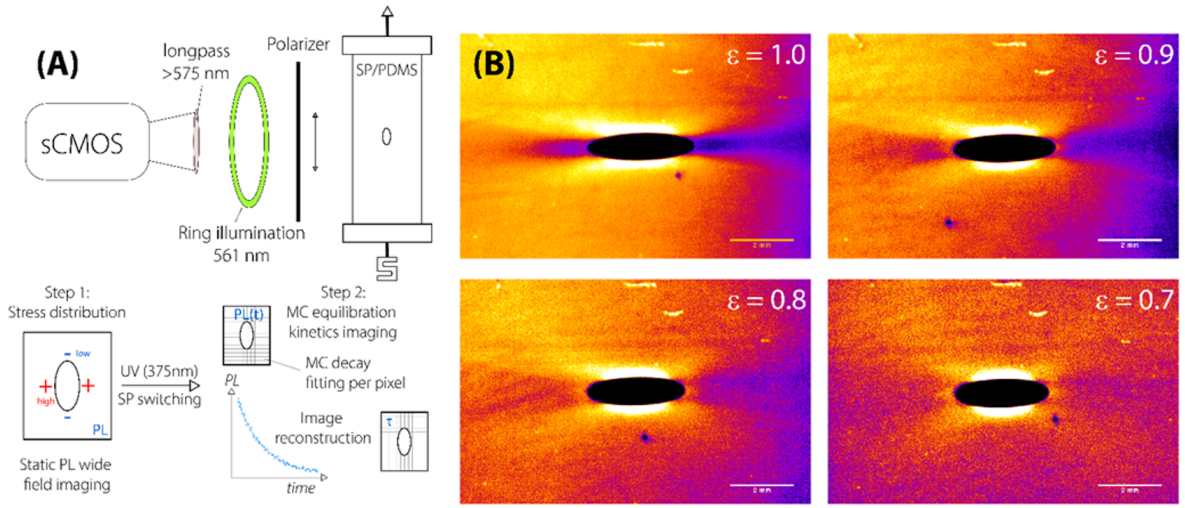

Figure 3.1: Diagram depicting the experimental process for the finding (left) and the photoluminescence intensity distribution at different strains(Right), adapted from [24]

Additionally, when considering the kinetics of the reaction, the researchers observed that upon relaxing the material from high strains (e.g. from 1.0 back to 0.5) the rate of the inverse, MC to SP, reaction depended on the history of the sample. Mechanically, the areas that had been more stretched exhibited faster conversion of MC to SP than the less stretched areas after relaxation. Under normal conditions these reactions slow down under high stress and UV exposure, but the opposite was observed, suggesting that the material's mechanical history may have prolonged effects on the kinetics of the reaction. These observations point to limitations in existing theoretical frameworks and motivate a deeper investigation into the relationship between mechanical loading, activation energy, and reaction kinetics in mechanochemical systems.

3.2. Research Questions and objectives

The present research is motivated by the need to establish a clearer mechanistic understanding of how mechanophore-based polymer systems, specifically spiropyran (SP) embedded in PDMS matrices, respond to externally applied strain. While previous studies have demonstrated the qualitative link between mechanical loading and mechanochemical activation, the quantitative relationship between local strain fields and photoluminescence response remains insufficiently characterized. Addressing this gap requires the integration and development of experimental methodologies that can simultaneously capture mechanical deformation and optical activation across multiple length scales.

Prior results indicate SP activation thresholds (strain/stress) and path-dependence under load/unload. However, a concurrent mapping of fluorescence and strain under controlled residual-stress conditions has not been developed. To this end the research questions have been developed as follows:

Research Question #1

What methodology can be employed to simultaneously correlate the mechanochemical activation and strain field?

Research Question #2

How does photoluminescence activation correlate with local strain field intensity in PDMS-based mechanophore systems?

The objective of this work is to design and validate an experimental framework that enables the direct comparison between strain evolution and mechanophore activation. This will be achieved by employing

DIC pictures to quantify the local strain distribution, while in parallel recording photoluminescence emission from the SP–MC transition. The combined analysis aims to uncover how localized deformation influences activation thresholds and reaction kinetics.

4

Methodology

The methodology for this study was directly motivated by observations of SP mechanophores behavior under mechanical loading, as detailed in Section 3.1. In summary, despite the absence of residual stress after unloading, persistent and regular fluorescence patterns were observed in samples previously strained beyond $\varepsilon \geq 0.5$ which remained stable, visible under polarized light aligned with the loading direction, but not across it. The kinetics of the MC-to-SP reverse reaction were found to vary spatially and to depend on prior strain history, with further stretched regions exhibiting faster recovery; these findings deviate from classical chemical-kinetics expectations, indicating a lasting effect of strain history.

4.1. Experimental Setup

4.1.1. Current Hardware

To explore these phenomena, the current setup, pictured in Figure 4.1, comprises of a custom-built mechanical testing rig integrated with a fluorescence imaging system, with a linear stage allowing for precise uniaxial tensile deformation of PDMS samples. Samples were illuminated using $532\,\mathrm{nm}$ light for excitation, and the emitted fluorescence from the merocyanine form was captured using a monochrome CMOS camera (Teledyne prime BSI) through a long-pass emission filter to isolate MC fluorescence from the light source.

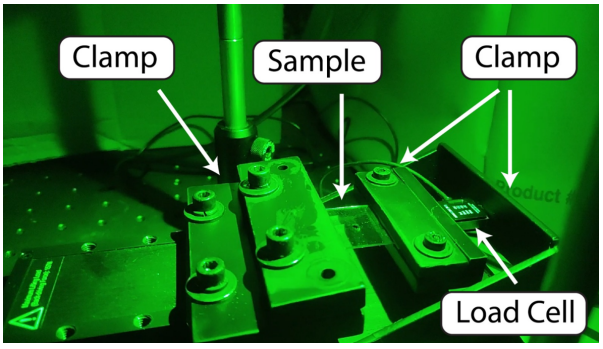

Figure 4.1: Experimental setup developed by Anuj Joshi for Master's thesis [19]

The setup was enclosed to minimize ambient light interference, ensuring consistent data acquisition. Samples were imaged during loading, relaxation, and UV-induced stages. Strain was applied in controlled steps, and high-resolution images were collected at each stage. Image acquisition and analysis was also incorporated into the system through custom Python scripts to quantify photoluminescence decay. This setup facilitated detailed, reproducible observation of both mechanical and photochemical behavior across multiple spatial and temporal scales.

Sample preparation

The sample preparation will follow the instructions given in this section to ensure reliable and repeatable testing. The SP molecules will be covalently bonded to the PDMS through the introduction of crosslinking agents during the preparation stage. The PDMS base is a viscous, short-chained polymer that terminates in vinyl groups, while its curing agent is a low-viscosity liquid that catalyses the polymerization. These are mixed in a ratio of 10:1, PDMS base:curing agent, made in square dishes for a $1\,\mathrm{mm}$ sample thickness.

Using $10\,\mathrm{g}$ of the Sylgard PDMS base, approximately $1\,\mathrm{g}$ of Sylgard 184 curing agent, and $20\,\mathrm{mg}$ of SP dissolved in $1\,\mathrm{mL}$ of toluene. The components are thoroughly agitated and then degassed in a vacuum desiccator; the mixture was poured into molds and cured at $85\,^{\circ}\mathrm{C}$ for approximately 2.5 hours. Additionally, a limitation identified in the previous research is that the fluorescence emitted by the MC molecules during reaction reflects in the bulk of the polymer. As it encounters the boundary layer, the change in refraction index from PDMS to air causes a halo of scattered light to form around the hole. To avoid this, two non-reflective glass slides will be placed covering the hole and a mixture of glycerol ($73\,\%$) and water ($23\,\%$), with the same refraction index as PDMS, will be added .

4.1.2. DIC integration

To enable DIC measurements, there is a need to integrate its capabilities into the existing hardware system. A key requirement for this process is the generation of a suitable speckle pattern on the sample surface, which plays a critical role in tracking deformation, and whose quality directly affects correlation accuracy. The conventional methods for speckle patterning (i.e., spray painting) have shown excessive variation in speckle size and spacing for reliable results. To address this limitation, several approaches are explored and will be further discussed. To ensure a reliable speckle pattern, some target parameters should be considered:

- an equivalent circular speckle diameter of 3–5 pixels,
- 40–$60\,\%$ areal coverage within the region of interest,
- image contrast of ≥ 50 gray levels on 16-bit images.

These targets follow established guidance and validations in the DIC literature [39, 13, 30, 31, 3].

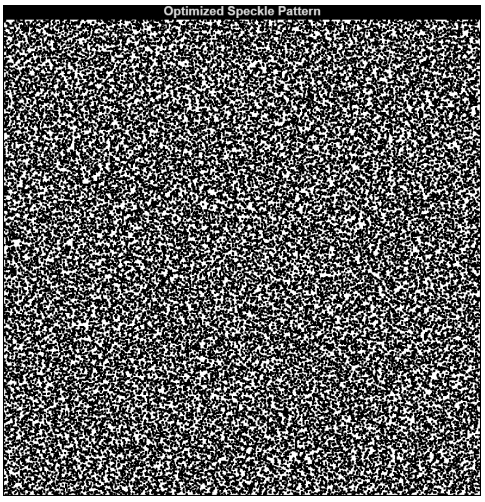

Figure 4.2: Speckle Pattern generated via Matlab script, specifications: 2048×2048 px sample, 32 px subsets, 12 dots per subset, radius of 10 px

For correlation analysis, software such as GOM Correlate, VIC-2D, or DICe are suitable options. Notably, Zeiss GOM Correlate [7] is based on algorithms validated in recent literature, including the work by Sales et al. [35], while VIC-2D [11] is recommended by Celestine. Figure 4.3 shows viability trials conducted on Zeiss GOM Correlate on sample DIC imagery.

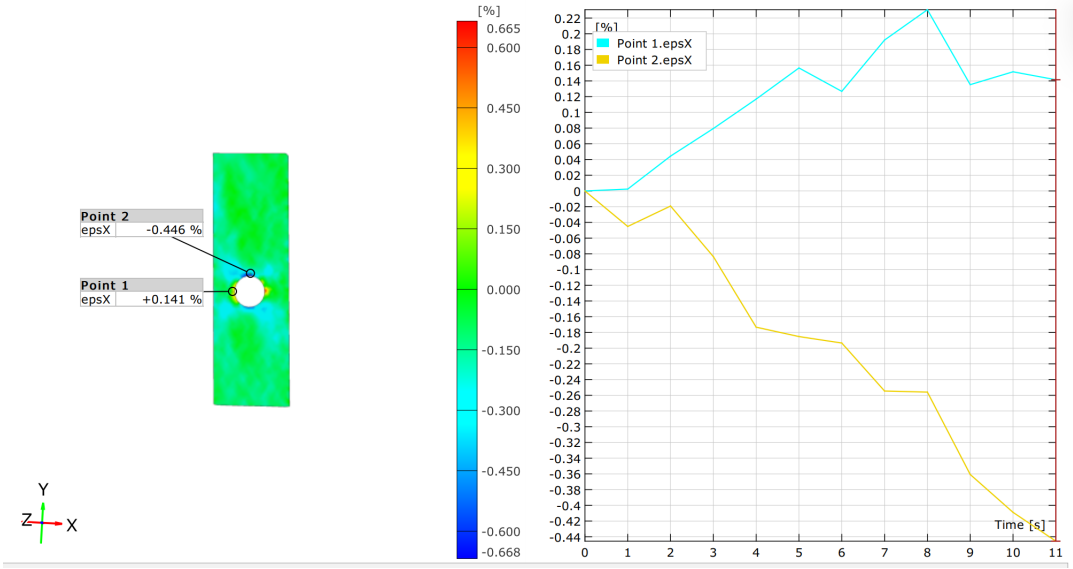

Figure 4.3: Proof of functionality of Zeiss GOM correlate software, on Zeiss provided reference images, shows correct distribution of strain around central hole

4.2. DIC process

In this study, PDMS was used for its hyperelastic mechanical behavior, with the intended strain range spanning 10–$100\,\%$. This necessitates a DIC approach capable of resolving both small and large deformations with adequate precision. While DIC is conceptually simple, the resolution and fidelity of strain measurements are highly sensitive to several interconnected parameters within the experimental setup. Strains will be reported as Green–Lagrange strain E for large deformations to ensure an appropriate mechanical description.

The camera configuration is fixed by the current hardware and therefore imposes constraints on sensor resolution, lens quality, magnification, and working distance. These parameters define the achievable spatial resolution and must remain consistent throughout the testing. Consequently, the primary variable influencing DIC quality is the speckle pattern applied to the sample surface. Optimal patterns require control over areal coverage (density), speckle size distribution, and contrast to ensure feature detectability across the full strain range without loss of correlation. Subset and step sizes will be selected relative to the speckle diameter (e.g., subsets ≥ 3–5 speckle diameters; step ≈ 0.5 of the subset) to maintain uniqueness and robustness under large strains.

Additionally, compatibility between the speckle-patterning ink and the PDMS substrate is essential. The ink must not chemically interact with or mechanically alter the elastomer surface, which could introduce spurious strain artifacts. Sample dimensions further influence pattern requirements: smaller specimens necessitate finer speckles and higher pattern densities, whereas larger samples allow for coarser distributions. As sample size and imaging scale are fixed by the optical setup, the speckle application method will be adapted accordingly to maintain subpixel correlation performance.

4.2.1. Speckle Pattern Application

Transfer Paper

Transfer paper was initially considered for speckle pattern application due to its simplicity and potential for transferring pre-designed patterns. However, most commercial inkjet printers have a poor pixel-wise resolution, which is below the threshold required for reliable speckle pattern application. This limitation results in, poorly defined speckles that hinder accurate displacement tracking. Despite these concerns, the method was tested to confirm its practical limitations through thermal printing and transfer paper, commonly used in tattoo applications. To evaluate the viability, professionals experienced in such techniques from SapphireInk tattoo Studio located in Delft, the Netherlands were consulted. Figure 4.4 shows the printed speckle pattern. Testing proved this method to be too inconsistent in quality and

adhesion to the sample was also limited.

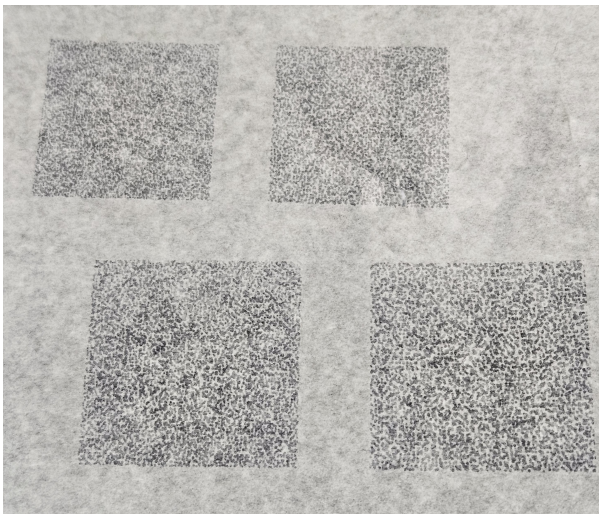

Figure 4.4: Speckle Pattern printed on transfer paper utilizing a thermal printer

Stamp

To improve pattern control and repeatability, a stamp-based approach was developed, drawing inspiration from commercial speckle kits such as those offered by Correlated Solutions. Using SolidWorks, stamps of various sizes were designed with randomized dot distributions to mimic the stochastic nature required for DIC. These stamps were fabricated using high-resolution Formlabs Form 3B+ and Form 4 printers, using Formlabs Tough 1500 Resin to ensure both precision and mechanical durability. This method provided a promising balance between repeatability and customization, particularly suitable for samples with smaller surface areas.

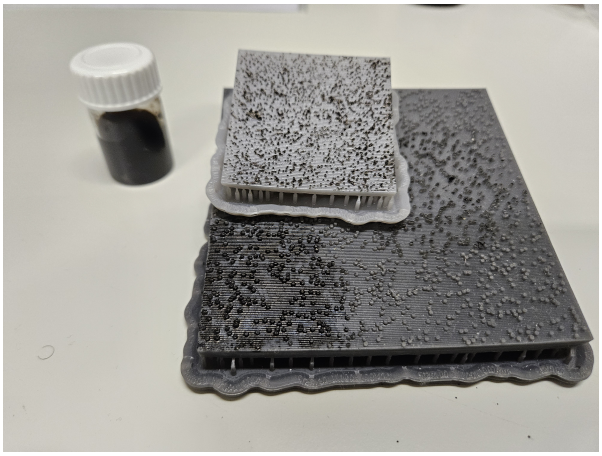

Figure 4.5: 3D printed stamps, vial of carbon-black paint

Spray paint

Spray paint was tested as a scalable solution for larger samples, typically those exceeding $50\,\mathrm{mm} \times 50\,\mathrm{mm}$. However, the method proved highly sensitive to the application technique. Variations in spraying distance, pressure, and nozzle type significantly affected the resulting speckle quality. Over 50 samples were evaluated using this approach, but most patterns lacked the necessary resolution for meaningful DIC analysis. While these trials helped verify the software's capability to process speckle images, the results were generally insufficient for quantitative strain measurements.

Airbrush

Airbrushing emerged as the most promising technique for producing high-resolution, high-contrast speckle patterns. This method was consistently recommended by experienced researchers, including Celestine [8] and Andrei Anisimov (AE, TU Delft), due to its widespread use in DIC applications. While highly effective, airbrushing has a steep learning curve and requires investment in specialized equipment. Mastery of the technique is essential to achieve repeatable and reliable results, but its advantages in speckle quality and control make it the preferred method in experimental mechanics.

(a) Airbrushed speckle pattern **(b)** Harder & Steenbeck's Evolution CR Plus Airbrush

Figure 4.6: Airbrushing equipment and sample

To spray on a speckle pattern a specific technique was utilized; the airbrush was set to the smallest nozzle opening, limiting the amount of paint flowing through. Then a flat surface was placed in front of the spray angling toward the sample, in small sprays the dye was bounced off of the flat surface onto the sample. this allows for the larger aerosols to stick to the flat surface while the small ones reach the sample.

4.3. Fluorescence imaging

The objective of this study is to investigate the relationship between the strain distribution and the activation of SP, therefore the fluorescent pattern must be imaged and tracked accordingly. The conversion of colorless SP to fluorescent MC occurs if sufficient energy is supplied to the system, possible both through UV-illumination and mechanical loading. The basis for this analysis relies on the absorption and emissions spectrum of SP and MC.

To analyze the activation patterns, it is important to understand the activation requirements for this process. MC exhibits an absorption maximum near $561\,\mathrm{nm}$, so using a $520\,\mathrm{nm}$ excitation light the molecule can be excited and become luminescent, as seen in figure 4.7. For mechanical activation, on the other hand, previous experimentation determined that the isomerization of SP into MC begins to occur at strains of 0.5 and rises until 1.0 [24]. These values were used the experimental bounds.

The luminescence of MC occurs at a range of wavelengths around $605\,\mathrm{nm}$; To highlight this emission the camera is equipped with a $575\,\mathrm{nm}$ long-pass filter [19]. While this range can vary slightly depending on the polymeric matrix SP is embedded in, sufficient validation with these values has been done with PDMS to verify this approach. This allows for the observation and analysis of the florescent activation of MC.

To correlate the strain field and fluorescent activation of MC the measurements must be taken concurrently and, ideally, synchronously to ensure direct and reliable correlation, such that the DIC imaging and light analysis can be performed at the same condition. This is important as many factors can influence the tests independently, such as the local material composition and general ambient light conditions, which limit the repeatability of the experiment. Therefore, a method must be derived for ensuring sufficient coverage of the sample for DIC purposes while allowing for the observation of lumi-

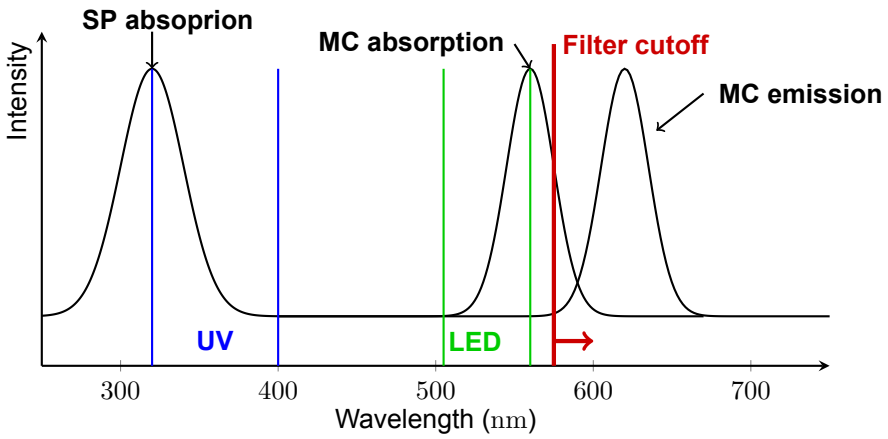

Figure 4.7: Absorption and emission spectrums for SP and MC; adapted from [19, 27]

nescence.

The main issue identified with this simultaneous correlation is the large intensity mismatch between MC fluorescence and the speckle patterns. This poses a compromise: illuminating the speckle pattern with a separate light source over saturates MC fluorescence, while not doing so reduces the feasibility of DIC. To mitigate this and allow for the analysis, a technique is required to allow both pattern to coexist, since favoring the intensity of either measurement would severely impact the other's attainable results.

4.3.1. Infrared Simultaneous Imaging

The planned DIC approach requires significant contrast to be accurate and provide a clear strain field of the sample, while, to observe the fluorescence, the sample is saturated by a green LED. Consequently, neither pattern is sufficiently separable during measurement, making the analysis impossible. This section describes the methodology developed from iterative testing and scrutiny of the experimental setup.

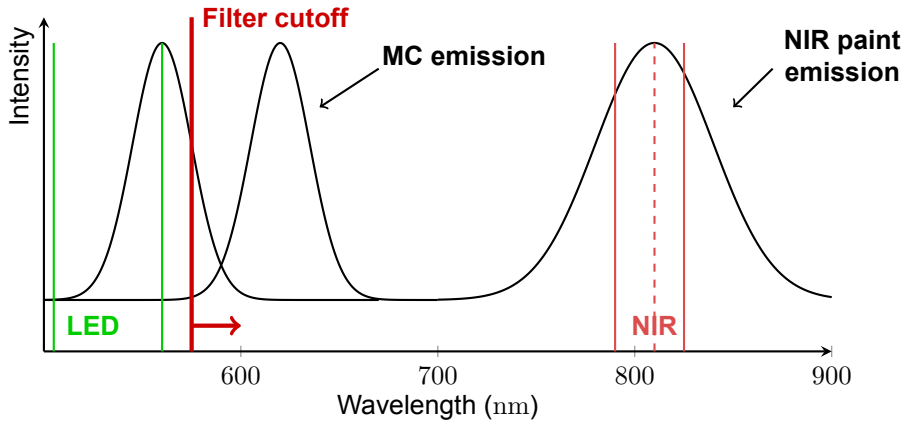

Figure 4.8: absorption and emission spectrums for MC and NIR imaging

To solve the issue a method of increasing the contrast between the pattern and the background is necessary without interfering with the luminescence emitted at $625\,\mathrm{nm}$ A bright $810\,\mathrm{nm}$ near-infrared (NIR) LED was chosen to illuminate the DIC pattern, as this wavelength is both detectable to the camera and not blocked by the long-pass filter (necessary to allow fluorescence observations). Such an illumination set up, however, drowns out any observable MC fluorescence. Alternating between green illumination for fluorescence observations, and NIR for DIC, allows for a near-simultaneous measurement of the two. To ensure that the DIC pattern is clearly visible, a NIR fluorescent dye will be used for for speckling.

This dye, namely IR-813 p-toluenesulfonate, has an excitation spectrum peaking at $813\,\mathrm{nm}$, translating to high fluorescent emission when illuminated with the NIR light, while being unaffected by the $525\,\mathrm{nm}$ green LED. The graphical visualization of this can be seen in Figure 4.8 and dye samples are shown in Figures 4.9a and 4.9b.

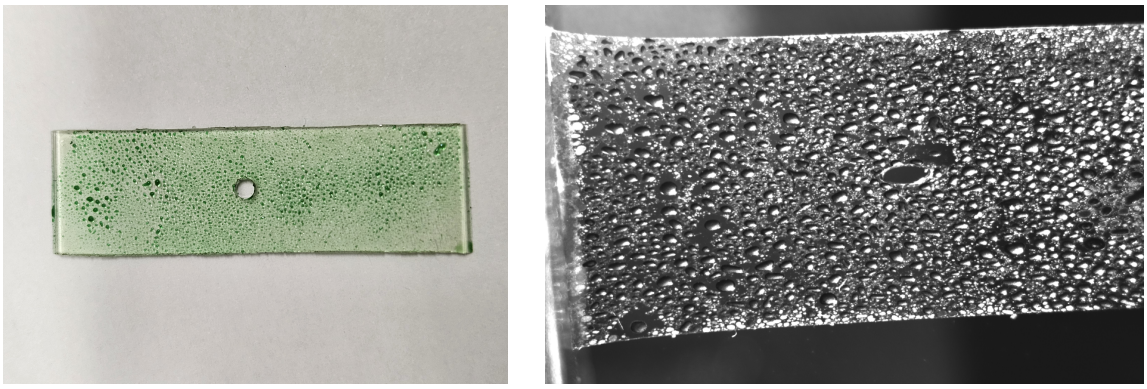

(a) NIR dye sample under natural light

(b) NIR dye sample under NIR LED

Figure 4.9: DIC sample

Significant consideration was given to the positioning of both the speckle pattern and the NIR LED, as their arrangement strongly influence the acquired images. For example, When the speckle pattern was place above the sample and illuminated from above, the fluorescent signal of MC was blocked by it, rendering the testing become unfeasible. Therefore to overcome this limitation the speckles were placed underneath the sample and the illumination was done from the top. This allowed from the NIR dye to fluoresce under the NIR LED while allowing full view of the fluorescence pattern of MC. Lastly, a spin coater was utilized to add a fine layer of PDMS to the sample surface, covering the speckle pattern, to protect the dye from the glycerol mixture that acted as a solvent.

5

Results

5.1. Final set-up and developed methodology

The final experimental configuration is shown in Figure 5.1, in which the NIR and green excitation LEDs are mounted with their respective driving circuits. The illumination control system is implemented on a breadboard, incorporating n-MOSFETs for controlling current flow to each LED. The MOSFETs are driven by an Arduino Uno via digital output pins, enabling rapid toggling between illumination sources. The circuit design and components are detailed in Appendix B.

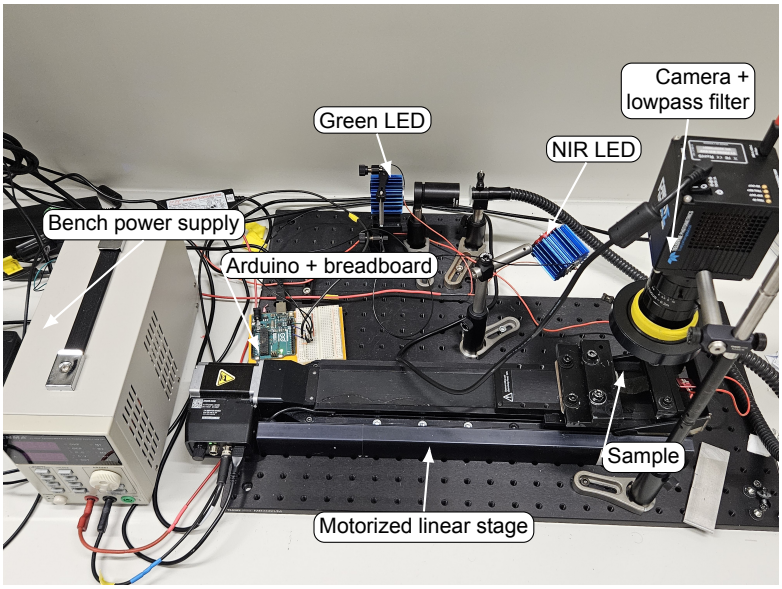

Figure 5.1: experimental set-up hardware

To enable automated and synchronized image acquisition, a BeanShell script was implemented within Micro-Manager (Appendix C). The script interfaces with the three primary hardware components: the motorized translation stage for applying controlled tensile strain, the CMOS camera, and the Arduino-controlled illumination module. The code first initializes all hardware, setting camera parameters and configuring stage velocity and acceleration. From user-defined strain parameters, it computes the stage motion profile and uses this information to set dynamic timeouts, ensuring each mechanical movement is completed before image capture.

During acquisition, the stage is first positioned at the initial strain value. For each strain increment, the sample is loaded quasi-statically, the stage advances to its new position and two consecutive images

are captured: one under green excitation and one under NIR illumination. The Arduino switches the LED state between exposures, guaranteeing that both channels correspond to the same mechanical state of the sample. This separation is critical for analysis, as it eliminates contamination between channels.

Because a large part of this thesis involved developing the experimental framework itself, a dedicated Appendix A has been included to document the software environment created for synchronized imaging and mechanical control. This appendix consolidates the configuration steps, user interface, and operational procedures required to run the integrated system. While the main text focuses on the methodological principles and results, the appendix ensures transparency and reproducibility, and serves as a practical reference for future adaptations of the setup.

5.2. Simultaneous imaging analysis

The developed methodology enabled synchronized acquisition of strain fields and mechanophore fluorescence by alternating illumination between green and NIR LEDs during each strain increment. This ensured that both imaging channels corresponded to the same mechanical state, eliminating temporal offsets while avoiding cross-contamination. Figures 5.2a and 5.2b demonstrate this capability at $100\,\%$ strain, capturing the fluorescent response of MC, after SP activation around the hole, and the speckle pattern.

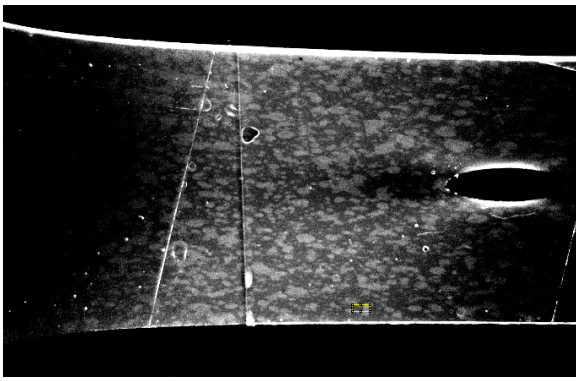

(a) Fluorescent pattern at 100% strain

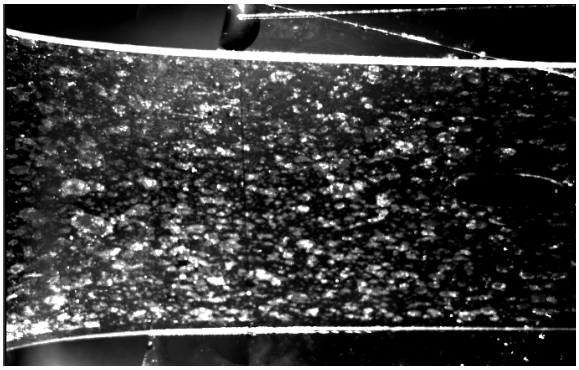

(b) Speckle pattern at 100% strain

Figure 5.2: Result of simultaneous imaging of MC fluorescence and speckle pattern

To evaluate the mechanochemical response, radial line profiles were extracted across the fluorescence images, allowing the intensity distribution to be quantified as a function of distance from the hole. This analysis was performed along both the main strain axis (horizontal/x-axis) and its perpendicular (vertical/y-axis), as it is anticipated that the y-axis profiles will exhibit higher peak intensities compared to the x-axis. This reflects the expected concentration of strain along the two axes. As previously discussed, fluorescence activation becomes visible at approximately $\varepsilon \approx 0.6$ and intensifies with increasing deformation, reaching a maximum near $\varepsilon \approx 1.0$. Correlated analysis is therefore presented at two maximum loading conditions (point of failure), 85% and 100% strain, which provide the clearest representation for assessing the relationship between local strain fields and spiropyran activation.

From here on, the area located above the hole, the one to the side of the central hole, and the average, will namely be referred to as axial, equatorial and average measurements, as shown in Figure 5.3.

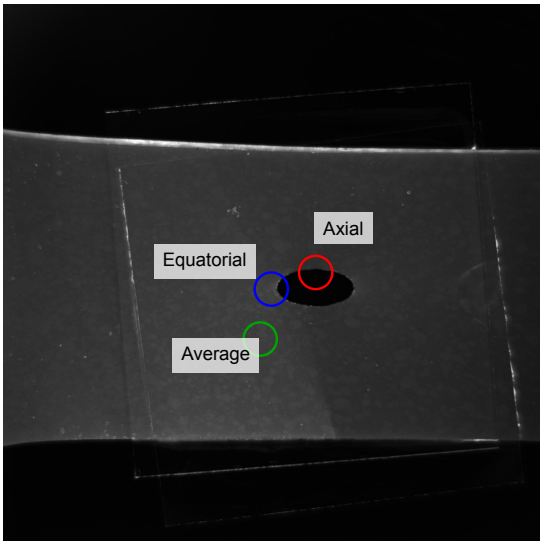

Figure 5.3: Annotated regions: axial strain region, equatorial strain region, and an average region.

5.3. Fluorescence pattern

To ensure validity, the analysis was performed on two samples; the most relevant results are presented in this section. The first sample measures $20\,\mathrm{mm} \times 45\,\mathrm{mm}$, and the second $40\,\mathrm{mm} \times 50\,\mathrm{mm}$, both with a central hole of $3\,\mathrm{mm}$ in diameter. These dimensions were selected one order of magnitude larger than the hole diameter, to approximate an infinite plate, keeping the strain field around the hole virtually unaffected by edge deformation.

This section presents results under green excitation at $520\,\mathrm{nm}$, obtained through the methodology detailed in Appendix A. The first two Figures, 5.4 and 5.5, show gray-level intensity over radial distance, measured from the hole center. The accompanying figures depict the radial line used for each profile. Next, analyses were performed at the theoretical extrema of the field: along the loading axis (axial), Figure 5.6, and along the transverse direction (equatorial), Figure 5.7, of the central hole. The gray level at a fixed point was plotted for each frame over the entire deformation. The same procedure was repeated for Sample 2. Radial line intensities are shown in Figures 5.8 and 5.9, and per-frame intensity traces are shown in Figures 5.10 and 5.11.

5.3.1. Sample 1: 20mm x 45mm

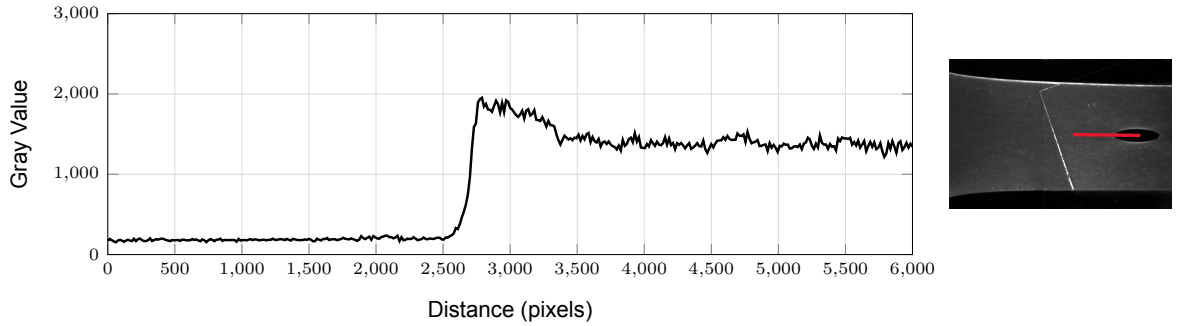

Figure 5.4: Sample 1: Fluorescence intensity in radial X-axis at 100% deformation.

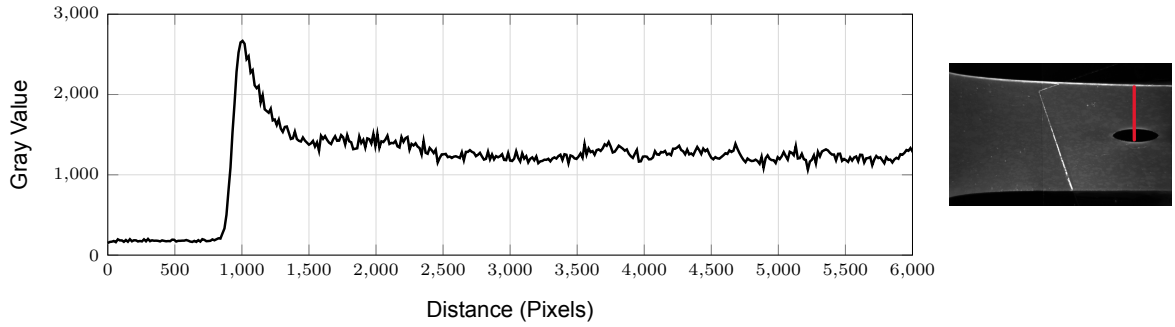

Figure 5.5: Sample 1: Fluorescence intensity in radial Y-axis at 100% deformation.

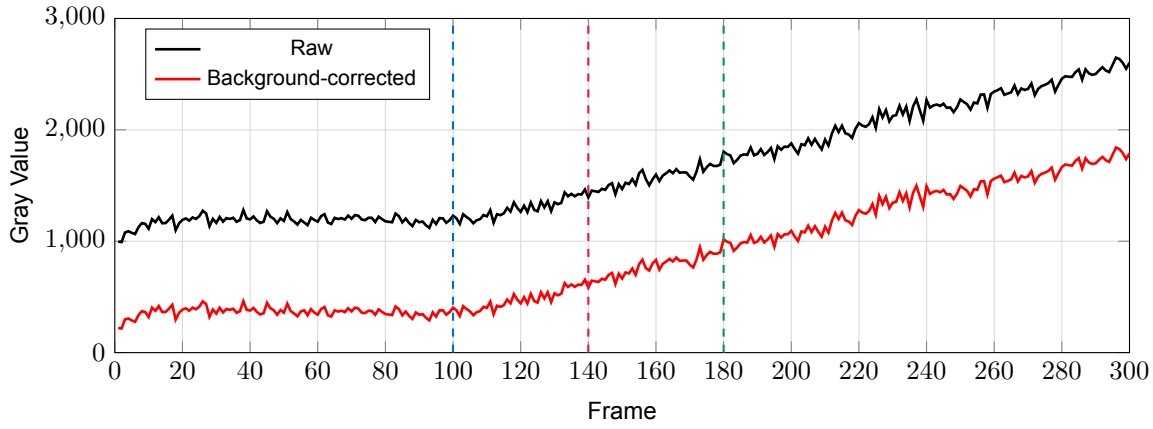

Figure 5.6: Sample 1: Axial area gray value over frame, with reference line at $x = 100$ and $x = 180$.

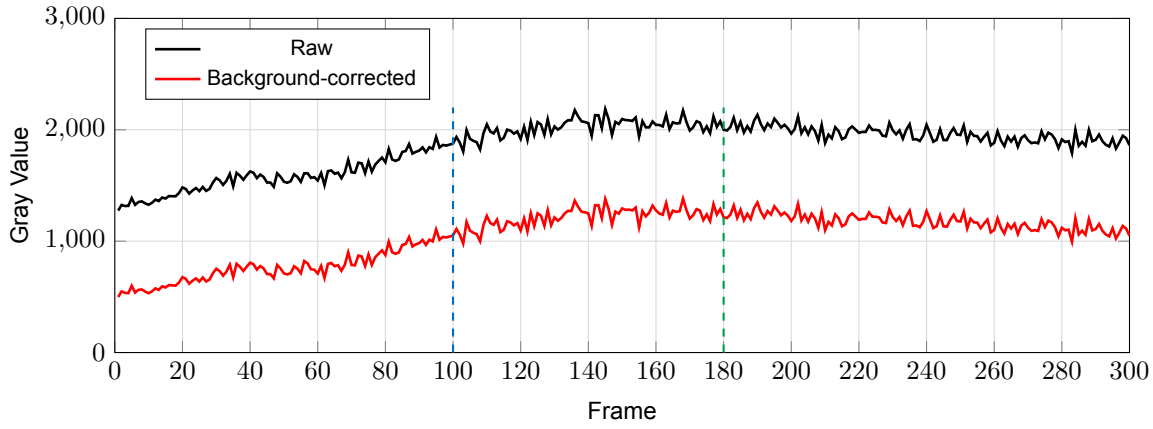

Figure 5.7: Sample 1: Equatorial area gray value over frame, with reference line at $x = 100$ and $x = 180$.

5.3.2. Sample 2: 30mm x 50mm

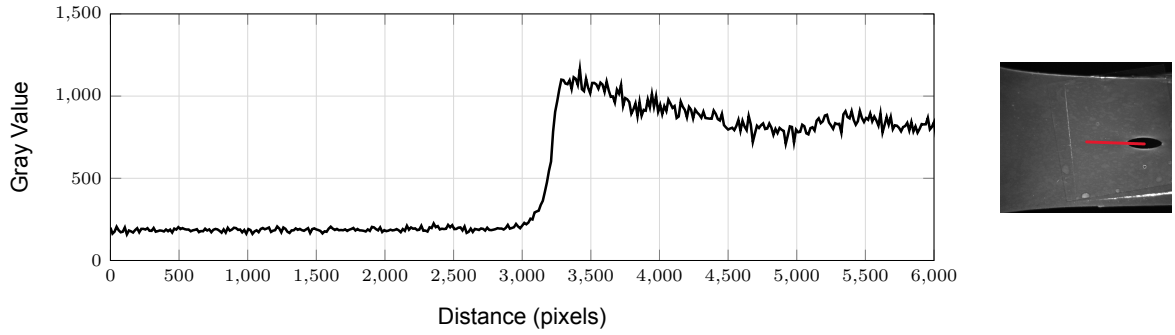

Figure 5.8: Sample 2: Fluorescence intensity in radial X-axis at 85% deformation.

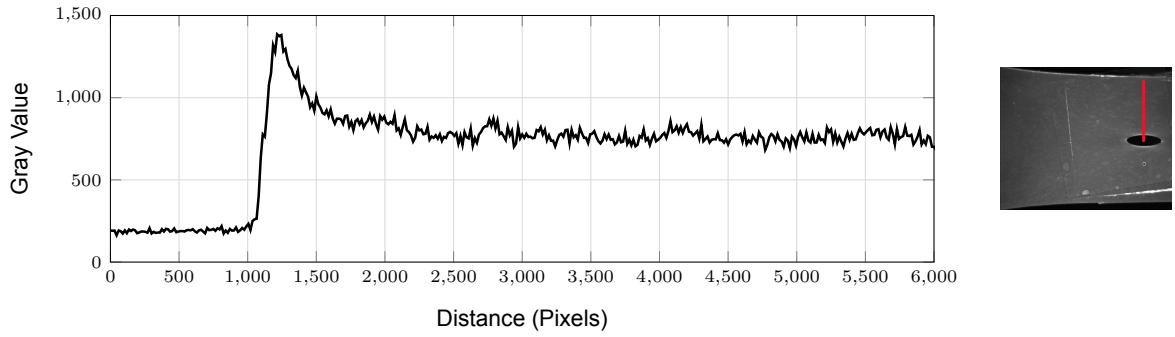

Figure 5.9: Sample 2: Fluorescence intensity in radial Y-axis at 85% deformation.

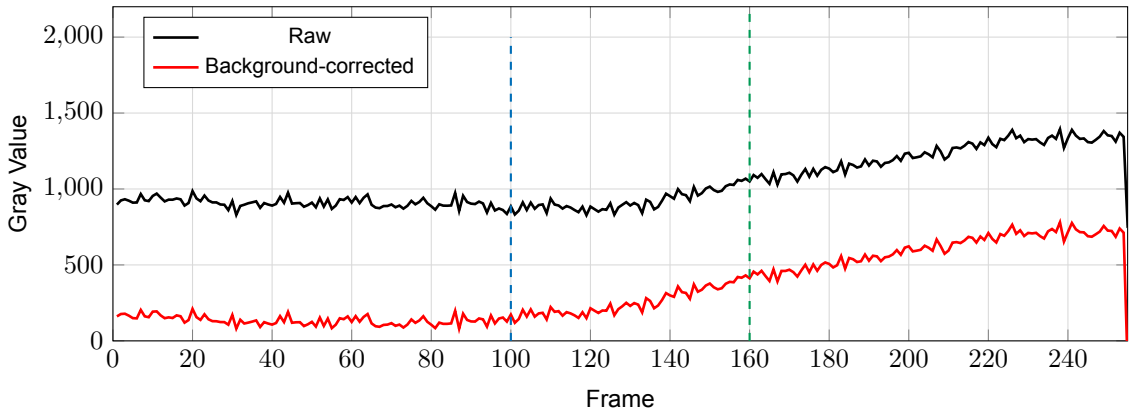

Figure 5.10: Sample 2: Axial area gray value over frame, with reference line at $x = 100$ and $x = 180$.

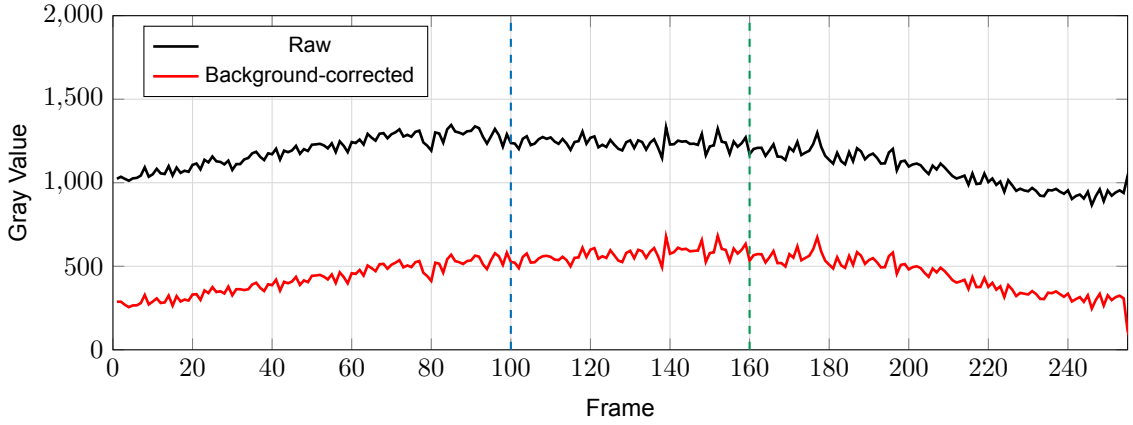

Figure 5.11: Sample 2: Equatorial area gray value over frame, with reference line at $x = 100$ and $x = 180$.

5.4. Correlation: Zeiss Gom correlate

This section shows the results of the Zeiss Gom correlate analysis for DIC, these correlate to the data acquired through the NIR imagery and respective dye, at a wavelength of $810\,\mathrm{nm}$. The 3D modelled DIC analysis can be seen in Figure 5.14, to extract direct correlation measurements Figures 5.12 and 5.13 present local strain (determine through Zeiss GOM correlate) in the same areas of interest as the fluorescence analysis, shown in Figure 5.3.

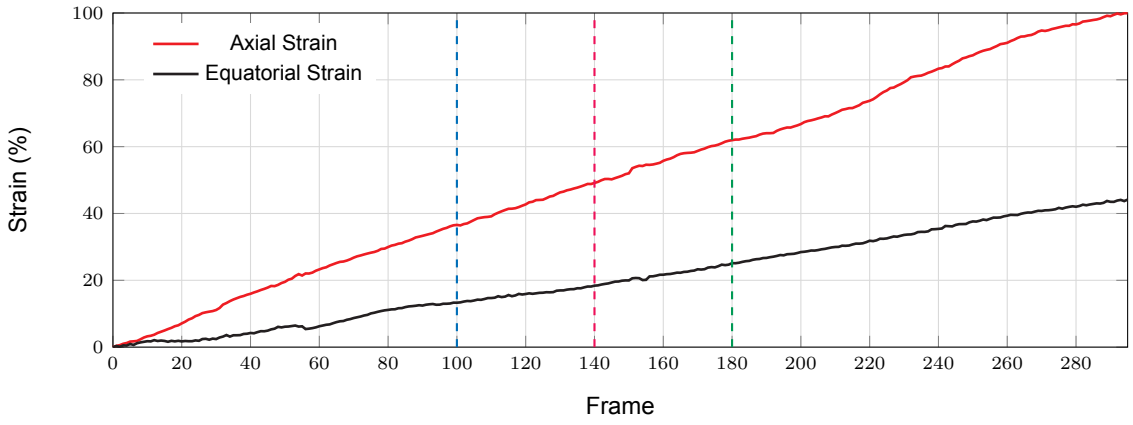

Figure 5.12: Sample 1 - Strain (%) over frame for Zeiss DIC0 with reference line at $x = 100$, $x = 140$ and $x = 180$.

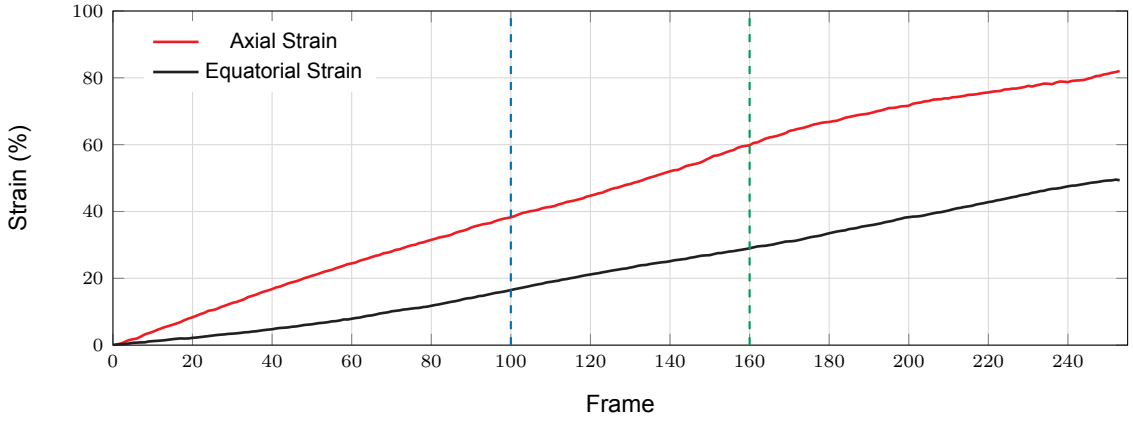

Figure 5.13: Sample 2 - Strain (%) over frame for Zeiss DIC0 with reference line at $x = 100$ and $x = 180$.

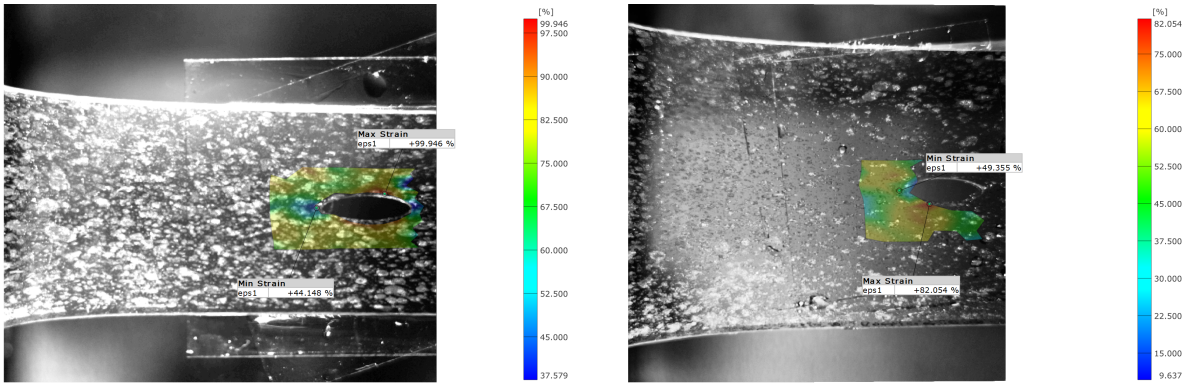

(a) Sample 1: 20 mm × 45 mm at 100% deformation.

(b) Sample 2: 30 mm × 50 mm at 85% deformation

Figure 5.14: Zeiss DIC 3D model of strain tensor for both samples

5.5. LoadCell Data

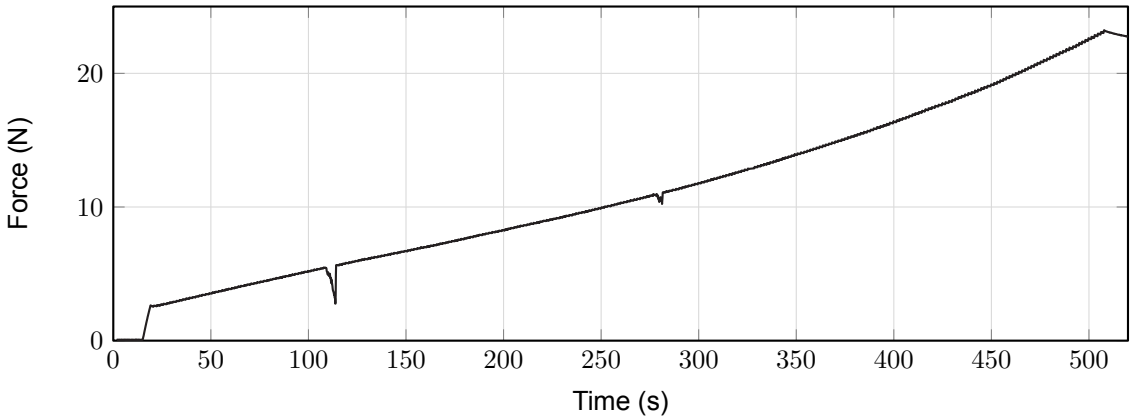

(a) Loadcell data for Sample 1 - Force(N) vs Time(s)

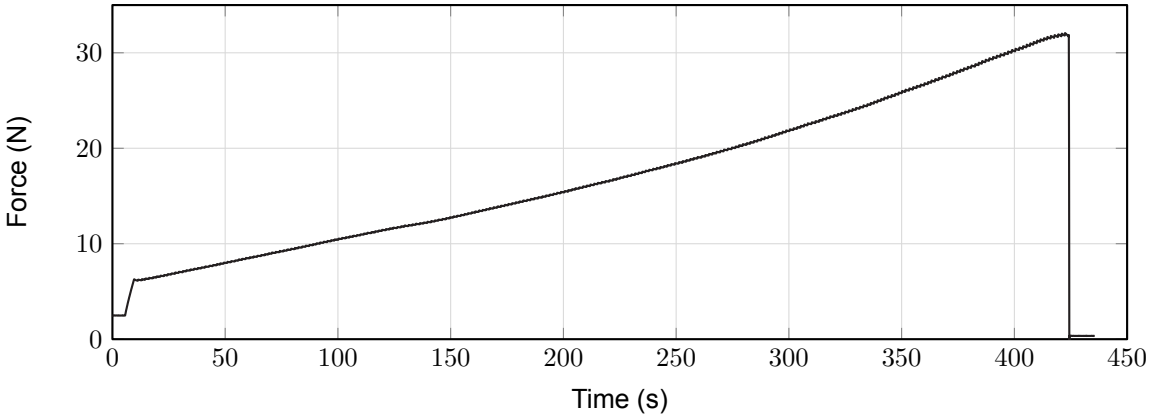

(b) Loadcell data for Sample 2 - Force(N) vs Time(s)

Figure 5.15: Loadcell data of experiments

6

Dicussion

The correlation between mechanical strain and fluorescence activation was examined by combining DIC strain concentration mapping, radial fluorescence profiles, gray value–frame histories, and load cell measurements. As expected, DIC analysis shows a pronounced strain localization in the axial region, with maximum strain increasing approximately linearly with the loading sequence (Figure 5.12). This localization guided the selection of points on the axial and equatorial areas for fluorescence analysis.

When comparing Figures 5.4 and 5.5, the radial profiles confirm anisotropy in the response. The peak intensity along the axial region is consistently higher than at the equatorial, within the expected stress concentration. The gray value measurements in the axial region over all frames shown in Figures 5.6 and 5.7, reveal distinct activation thresholds. Fluorescence onset is detected near frame 100 at 36.6% occurring at 7–$8\,\mathrm{N}$ tracked in Figure 5.15b, this is below baseline luminosity and is not visually observable. Sufficient intensity is reached at frame 140 around 11–$12\,\mathrm{N}$, becomes noticeable with the emergence of the characteristic ring, corresponding to 49.1%. It becomes visible to the naked eye by frame 180 at 61.9% strain and a corresponding force of 15–$16\,\mathrm{N}$. Maximum fluorescence at 100% strain coincides with the peak force of $\sim 23\,\mathrm{N}$.

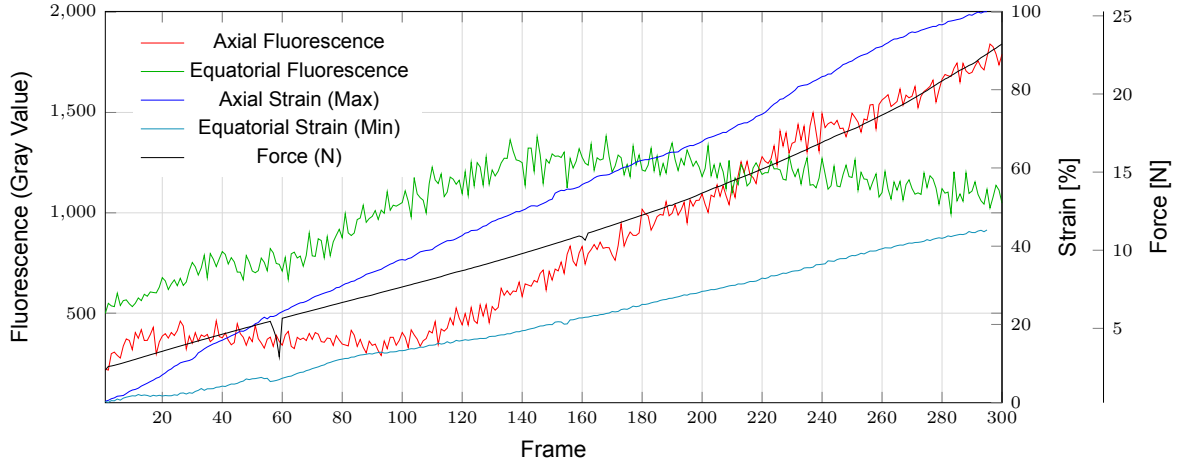

Figure 6.1: Fluorescence, strain, and force vs. frame for Sample 1.

When plotted in parallel with the DIC strain scale this is consistent with prior reports [24, 22]. With this confirmation, the strain graph shown in Figure 5.12 and the gray value response, Figure 5.6, enable direct frame to strain comparison. These aligned values, can be seen overlayed in Figure 6.1, which validates the methodology and establishes a reproducible linkage between applied load, local strain concentration, and mechanophore activation. A behaviour predicted in the highlighted literature by Haque [15] and Celestine [8].

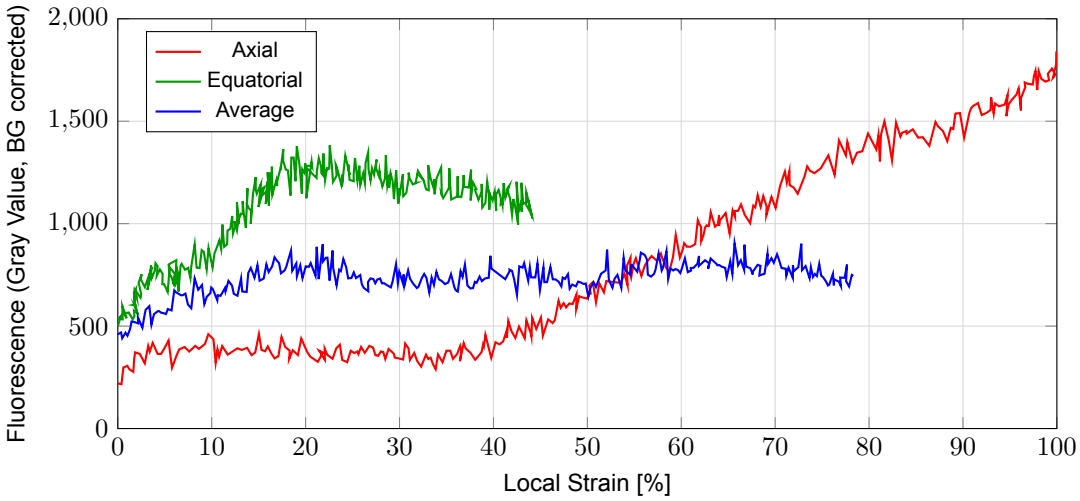

Figure 6.2: Fluorescence vs DIC Strain for Axial, Equatorial, and Average points for sample 1.

The graph shown in Figure 6.2 depicts the fluorescence activation plotted as a function of strain. Here it can be seen that the axial fluorescence activation has its rise at 40% and progresses linearly until 100%, comparatively the equatorial has a immediate increase in the gray value, peaking at 20%. The average point is taken sufficiently far from the hole that its impacts on the measurement are minimal, at this location an initial rise can be seen, which then plateaus. This initial response of either curve can not be attributed to SP activation so it is theorized that it is resulting from an external factor.

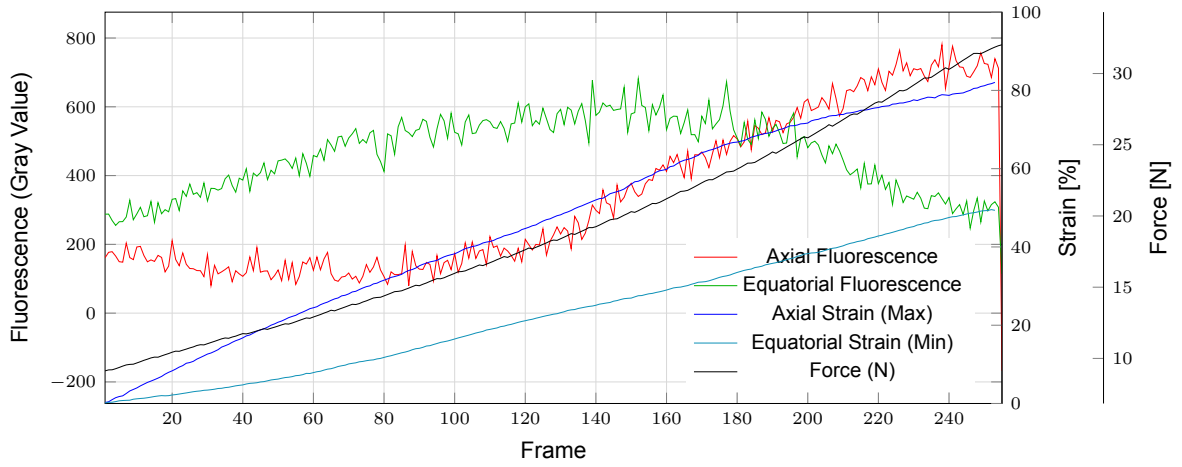

Figure 6.3: Fluorescence, strain, and force vs. frame for Sample 2.

The second sample showed a fluorescence response with notable differences compared to Sample 1. Radial line profiles seen in Figures 5.8 and 5.9, are taken at 85% deformation. In Figure 5.15b, the load-cell data of Sample 2 is shown, the sample experienced higher forces, with peak values exceeding $30\,\mathrm{N}$ due to its larger cross-section. It would be expected that the increased load would cause higher fluorescent peaks, however this does not occur, indicating that local stress distribution play a greater role in driving spiropyran activation.

The plot of gray value over frames for the axial region (Figure 5.10) reveals luminescence onset around frame 120, corresponding to a strain of $44.7\,\%$ and peaking at frame 160 ($59.8\,\%$). This trend is consistent with the correlation observed in Sample 1, but with a slightly earlier onset relative to the total strain level. For lower strains, variations in gray value are unlikely to reflect mechanophore activation, but rather experimental noise or background illumination effects. A similar trend is observed in the Equatorial fluorescence plots for both samples, rising up to $50\,\%$ strain and subsequently decreasing,

a trend that the current understanding of SP activation does not explain. Overall, congruence between Figures 5.6 and 5.7 and Figures 5.10 and 5.11 supports the reproducibility of the experiments. For ease of comparison, all measurements for sample 2 are overlayed in Figure 6.3.

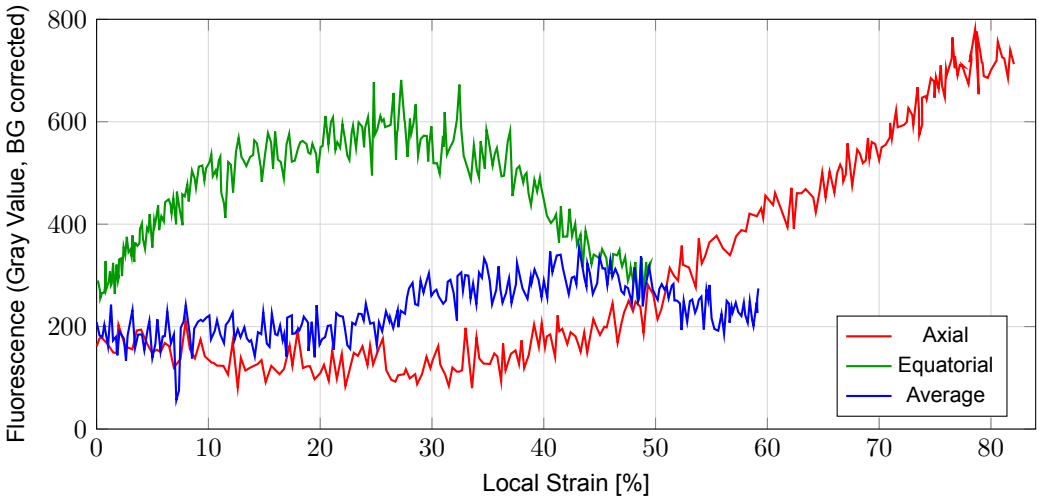

Figure 6.4: Fluorescence vs DIC Strain for Axial, Equatorial, and Average points for sample 2.

The plot in Figure 6.4 shows the fluorescence activation as a function of strain for Sample 2, similarly to Figure 6.2. Here a similar trend can be seen for the axial and equatorial points, where the first has an onset of activation at 40% while the latter rises immediately peaking around 20%. A slight difference is seen in the response of the average, maintaining a steady consistent value for the the full deformation. The axial curve, in both sample 1 and 2, share a strong resemblance to the curve presented in the work of Kim et al. [22] for the same range, showing an increase at around 50% strain for areas that reach the full global strain, additionally, the average strains maintaining a constant luminosity is consistent with regions of lower stress concentrations. the outlier stands in the equatorial values, where it is believed that a deviation in acquisition or optical effects causes the observed behavior.

Statistical correlation

To further compute the correlation between the strain and the fluorescent data, a statistics based, Pearson linear correlation is performed on the full scale data as well as low strain data, due to the behavior of the curves varying significantly. The goal is to assign a correlation score to the two datasets by summing the squares of the differences in magnitude for each attribute [5]. This produces a score whose magnitude indicates the correlation between the two datasets, and whose sign indicates either direct or inverse correlation, varying from − 1 to + 1. The Pearson linear correlation r between fluorescence (x) and local strain (y), where n is the total number of frames, is defined as:

$$r = \frac{\sum_{i=1}^{n}(x_i - \bar{x})(y_i - \bar{y})}{\sqrt{\sum_{i=1}^{n}(x_i - \bar{x})^2}\sqrt{\sum_{i=1}^{n}(y_i - \bar{y})^2}}, \tag{6.1}$$

The full Pearson coefficient between the axial fluorescence and strain was found to be $r = 0.949$, with a $95\,\%$ Confidence Interval of $95\%\ CI = [0.936, 0.959]$. While for low strains ($\leq 20\,\%$) the coefficient is $r = 0.447$, with a $95\%\ CI = [0.193, 0.645]$. The equatorial showed for full strain $r = 0.713$ with $95\%\ CI = [0.652, 0.765]$ and a low strain ($\leq 15\,\%$) of $r = 0.942$ with $95\%\ CI = [0.917, 0.960]$. The data suggests that the equatorial fluorescence tracks strain tightly at low strain, whereas the axial channel attains very high linear coupling only when the full range is considered

For the second sample the Pearson coefficient was also determined.For the Axial fluorescence and strain the full Pearson coefficient was found to be $r = 0.898$, for a Confidence Interval(CI) of 95% this value can range between 0.872 and 0.920. While for low strains ($\leq 15\,\%$) the coefficient is -0.585, 95% ranging -0.747 and -0.358. The equatorial showed for full strain $r = 0.075$ with $95\%\ CI = [-0.049, 0.196]$

and a low strain ($\leq 15\,\%$) of$r = 0.943$ with $95\%\ CI = [0.915, 0.962]$. Compared to Sample 1, the same qualitative pattern holds: equatorial correlation is strongest in the low-strain regime, while axial correlation becomes strong when the full range is considered; the negative axial at low-strain r indicates a lack of linear co-variation in that early regime.

7

Conclusion

7.1. Main Findings

Research Question #1

What methodology can be employed to simultaneously correlate the mechanochemical activation and strain field?

A dual-imaging methodology was developed that integrates fluorescence imaging with DIC under the same loading conditions. The approach used alternating green ($532\,\mathrm{nm}$) and near-infrared ($810\,\mathrm{nm}$) illumination, controlled by an Arduino system, to capture fluorescence activation and speckle patterns at the same mechanical state of the sample. This eliminated temporal offsets and allowed direct overlay of fluorescence intensity maps, DIC strain fields, and load cell measurements. By extracting radial fluorescence profiles and synchronizing them with strain concentration maps, the methodology provided a reproducible framework to correlate mechanochemical activation with strain. Although some artifacts were observed in low-strain regimes were not explained by the current understanding of SP in hyperelastic polymers, the method proved robust for full-field strain–activation correlation and can be generalized for other mechanophore-containing systems

Research Question #2

How does photoluminescence activation correlate with local strain field intensity in PDMS-based mechanophore systems?

The experiments demonstrate that photoluminescence activation of spiropyran in PDMS coincides with regions of high local strain intensity. DIC consistently shows strain localization along the axial direction of the central hole, and fluorescence onset is observed at these same regions. For example, in Sample 1, fluorescence became detectable at 36.6% strain and intensified linearly with increasing load, reaching unaided visibility around 61.9% strain and peaking at full deformation. Statistical analysis reinforced this link, with high Pearson coefficients (e.g., $r = 0.949$ for axial fluorescence vs. strain in Sample 1), confirming a near-linear correlation at full strain levels, while at low strains the correlation was weaker or inconsistent

7.2. Research Limitations

Several limitations inherent to the experimental set-up and methodology constrained the scope and reliability of this study. In the attempt to aid future developments within this project this section compiles the limitations most prevalent and, at points, suggests possible mitigations that, due to time constraints, were not applied.

Quality and Resolution First, the DIC technique employed is inherently optimized for large sample

sizes and relatively small deformations. This characteristic imposed restrictions on the level of accuracy and resolution achievable, thereby influencing the results. Moreover, DIC is highly sensitive to operator-dependent factors; significant training and practice are required to minimize human error, which reduces repeatability and consistency across measurements.

Another key limitation relates to the subset-based functioning of DIC discussed in Section 2.5.3, which operates at the pixel level. Given the finite speckle size achievable with the technique implemented and sample size, certain information is inevitably lost, reducing the fidelity of strain mapping. To further reduce the scale of the speckle pattern a finer aerosol distribution system can be utilized with more consistent speckle generation and sample coverage, this would considerably improve the capabilities of DIC in the system.

Data contamination In terms of fluorescence analysis, quantification of the fluorescent response remains sensitive to background intensity variations, photobleaching, and uneven illumination from the excitation source. Additionally, grayscale analysis revealed fluctuations beyond the central region of interest, these artifacts are likely induced by the speckle pattern itself.

These factors may have introduced systematic error in correlating fluorescence activation with strain. Furthermore, variability across individual samples, arising from differences in preparation, coating uniformity, and clamping alignment, adds uncertainty to the findings. Additionally, environmental factors, particularly uncontrolled light fluctuations, were found to significantly skew fluorescence measurements and DIC accuracy. This was most evident in the disruption observed for Sample 2 in Figure 5.10, highlighting the importance of isolating the testing environment for precision experiments.

Experimental limitations Some limitations came from the pre-existing experimental set-up described in Section 4.1.1, where the mechanical boundary conditions introduced uncertainties. The clamping forces applied to the samples could not be uniformly distributed causing inconsistencies to influence strain distributions. Small spacers can be implemented to mitigate the uneven compression and maintain plate alignment. An additional limitation arises from the electrical configuration of the illumination system. The NIR LED used for DIC imaging and the green LED used for fluorescence excitation required different current levels to achieve optimal performance. However, due to the reliance on a single shared power supply, a compromise operating point had to be established to balance both sources. This equilibrium setting reduced the effective output quality of each LED, leading to suboptimal illumination conditions, a simple fix that should be implemented for future iterations.

7.3. Future recommendations

To address these limitations and strengthen the methodology, several recommendations are proposed. First, improvements to the clamping system and illumination circuit are essential. Uniform distribution of clamping loads can be better achieved by integrating precision-aligned fixtures or incorporating compliant spacers designed specifically for polymer samples. For the optical system, providing independent power supplies for the NIR and green LEDs would eliminate the need for compromise operating points, ensuring both sufficient fluorescence excitation and high-contrast DIC imaging. Additionally, the application of the speckle pattern can be improved by the use of fine aerosols dispersers such as those utilize in aerosol vaccine technologies. The resulting, smaller and more evenly spread speckles would significantly improve the DIC accuracy, regardless of the software selected.

In terms of strain analysis, reliance on Zeiss GOM Correlate should be replaced with more robust approaches as during analysis, the accuracy of results were deemed questionable. This is due to its means of calculating the strain field and its lack a pure numerical data, critical for validation. Therefore, this limitations prevents it from serving as the primary basis for strain field determination. To ensure a more reliable evaluation, the visual strain mapping should instead be conducted using a software which gives access to this information.

Because of the mentioned resolution limitations and sample size, it is believed that an open source and/or custom made DIC would be the most optimal solution, allowing for custom speckle calculation. Alternatively, the two-dimensional Finite Element Global Digital Image Correlation (FE-DIC) framework developed by Jin Yang is reliable. This method applies a finite element mesh to the displacement field, improving robustness against noise and enabling global consistency in the computed strain maps.

The use of sample specific meshes allows for high order correlation and more reliable deformation calculation.The Mesh can easily be developed by following the work of Jiexian Ma [26]. This can provide more accurate results as it allows for vector extrapolation of the Greens-Lagrage strain tensor, unlike Zeiss Gom Correlate. The use of FE-DIC would strengthen the validity of the correlation analysis.

References

[1] Sergey Akbulatov and Roman Boulatov. “Experimental Polymer Mechanochemistry and its Interpretational Frameworks”. In: *ChemPhysChem* 18.11 (2017), pp. 1422–1450. DOI: https://doi.org/10.1002/cphc.201601354. eprint: https://chemistry-europe.onlinelibrary.wiley.com/doi/pdf/10.1002/cphc.201601354. URL: https://chemistry-europe.onlinelibrary.wiley.com/doi/abs/10.1002/cphc.201601354.

[2] Y. Bai and T. Wierzbicki. “Application of Extended Mohr–Coulomb Criterion to Ductile Fracture”. In: *International Journal of Fracture* 161 (2010), pp. 1–20. DOI: 10.1007/s10704-009-9422-8.

[3] T. A. Berfield et al. “Micro-and nanoscale deformation measurement of surface and internal planes via digital image correlation”. In: *Experimental Mechanics* 47 (1 Feb. 2007), pp. 51–62. ISSN: 00144851. DOI: 10.1007/s11340-006-0531-2.

[4] Thomas A. Berfield et al. “Fluorescent image correlation for nanoscale deformation measurements”. In: *Small* 2 (5 May 2006), pp. 631–635. ISSN: 16136810. DOI: 10.1002/smll.200500289.

[5] J.J. Berman. *Data Simplification: Taming Information with Open Source Tools*. Morgan Kaufmann, 2016. DOI: https://doi.org/10.1016/C2015-0-00783-3.

[6] H.A. Bruck et al. “Digital Image Correlation Using Newton-Raphson Method of Partial Differential Correction”. In: *Proceedings of the 1988 SEM Spring Conference on Experimental Mechanics*. Portland, OR: Society for Experimental Mechanics, 1987.

[7] Carl Zeiss Industrial Metrology LLC. *ZEISS Correlate Software*. https://www.zeiss.com/metrology/en/software/zeiss-correlate.html. Accessed: 2025-06-05. 2025.

[8] Asha Dee N. Celestine, Nancy R. Sottos, and Scott R. White. “Strain and stress mapping by mechanochemical activation of spiropyran in poly(methyl methacrylate)”. In: *Strain* 55 (3 June 2019). ISSN: 14751305. DOI: 10.1111/str.12310.

[9] Y. Chen. “The Unique Geometry of Mechanophore Activation in a Rotaxane Force Actuator”. In: *Journal of the American Chemical Society* 146.24 (2024). Epub ahead of print, pp. 16381–16384. DOI: 10.1021/jacs.4c05168.

[10] Anna Christianson. *Chem 104*. Open Educational Resource (OER) on LibreTexts. Course material published on LibreTexts, compiled on 2025-04-11. 2025. URL: https://chem.libretexts.org/Courses/Bellarmine_University/BU%3A_Chem_104_%28Christianson%29.

[11] Correlated Solutions Inc. *VIC-2D: Digital Image Correlation Software*. https://www.correlatedsolutions.com/vic-2d. Accessed: 2025-06-05. 2025.

[12] Naomi Deneke, Mitchell L. Rencheck, and Chelsea S. Davis. *An engineer’s introduction to mechanophores*. July 2020. DOI: 10.1039/d0sm00465k.

[13] Y. L. Dong and B. Pan. “A Review of Speckle Pattern Fabrication and Assessment for Digital Image Correlation”. In: *Experimental Mechanics* 57 (8 Oct. 2017), pp. 1161–1181. ISSN: 17412765. DOI: 10.1007/s11340-017-0283-1.

[14] Bruno M. Fanconi. “Chain scission and mechanical failure of polyethylene”. In: *Journal of Applied Physics* 54.10 (Oct. 1983), pp. 5577–5582. ISSN: 0021-8979. DOI: 10.1063/1.331814. eprint: https://pubs.aip.org/aip/jap/article-pdf/54/10/5577/18402797/5577_1_online.pdf. URL: https://doi.org/10.1063/1.331814.

[15] Nazmul Haque et al. “Quantifying Localized Stresses in the Matrix of a Fiber□Reinforced Composite via Mechanophores”. In: *Macromolecular Chemistry and Physics* 224.24 (2023), p. 2300298. DOI: 10.1002/macp.202300298. URL: https://doi.org/10.1002/macp.202300298.

[16] William F Hosford. *Mechanical Behavior of materials*. 2nd edition. Cambridge University press, 2010. ISBN: 978-0-511-65836-5.

[17] Richard Janissen and Georgy A. Filonenko. “Mechanochemistry of Spiropyran under Internal Stresses of a Glassy Polymer”. In: *Journal of the American Chemical Society* 144 (50 Dec. 2022), pp. 23198–23204. ISSN: 15205126. DOI: 10.1021/jacs.2c11280.

[18] M. Janssen, J. Zuidema, and R.J.H. Wanhill. *Fracture Mechanics*. Delft, The Netherlands: VSSD, 2002, pp. xii + 365. ISBN: 90-407-2221-8. URL: http://www.vssd.nl/hlf/m004.htm.

[19] Anuj Joshi. “Correlating Fluorescence and Stress/Strain for Spiropyran Mechanosensors”. Supervised by Siddhant Kumar and Georgy A. Filonenko; coaching by M. K. Ghatkesar. Master’s thesis. Faculty of Mechanical Engineering: Delft University of Technology, 2024.

[20] William D. Callister Jr and David G. Rethwisch. *Callister’s Materials Science and Engineering*. John Wiley & Sons, 2020. ISBN: 978-1-119-40549-8.

[21] Sahoo N. Karuppasamy K. Balaji P. S. *Applications and Techniques for Experimental Stress Analysis*. IGI Global, 2020. DOI: 10.4018/978-1-7998-1690-4.

[22] Tae Ann Kim et al. “Mechanical Reactivity of Two Different Spiropyran Mechanophores in Polydimethylsiloxane”. In: *Macromolecules* 51.22 (Nov. 2018), pp. 9177–9183. DOI: 10.1021/acs.macromol.8b01919.

[23] Luuk Kortekaas and Wesley R. Browne. *The evolution of spiropyran: Fundamentals and progress of an extraordinarily versatile photochrome*. June 2019. DOI: 10.1039/c9cs00203k.

[24] Sid Kumar, Georgy A. Filonenko, and Anuj Joshi. “Dynamic Mechanochemical Memory in Imaging Stress History and Heterogeneity in Elastomers”. Manuscript in preparation. 2025.

[25] Meng Li et al. “Let spiropyran help polymers feel force!” In: *Progress in Polymer Science* 79 (2018), pp. 26–39. ISSN: 0079-6700. DOI: https://doi.org/10.1016/j.progpolymsci.2017.11.001. URL: https://www.sciencedirect.com/science/article/pii/S0079670017301478.

[26] J. Ma and Y. Li. *Im2mesh: A MATLAB/Octave package for generating finite element mesh based on 2D multi-phase image*. Version 2.1.5. 2025. DOI: 10.5281/zenodo.14847059. URL: https://doi.org/10.5281/zenodo.14847059.

[27] R. Ramos-Garcia et al. “Polarization dependence on the holographic recording in spiropyran-doped polymers”. In: *Optical and Quantum Electronics* 35.6 (May 2003), pp. 641–650. ISSN: 1572-817X. DOI: 10.1023/A:1023964804048.

[28] Neil K. Razdan, Ting C. Lin, and Aditya Bhan. “Concepts Relevant for the Kinetic Analysis of Reversible Reaction Systems”. In: *Chemical Reviews* 123.6 (2023). PMID: 36802557, pp. 2950–3006. DOI: 10.1021/acs.chemrev.2c00510. eprint: https://doi.org/10.1021/acs.chemrev.2c00510. URL: https://doi.org/10.1021/acs.chemrev.2c00510.

[29] Phillip Reu. *Stereo-rig design: Camera selection-part 2*. Nov. 2012. DOI: 10.1111/j.1747-1567.2012.00872.x.

[30] Phillip Reu. *Stereo-rig design: Creating the STEREO-RIG LAYOUT - PART 1*. Sept. 2012. DOI: 10.1111/j.1747-1567.2012.00871.x.

[31] Phillip Reu. “Stereo-rig design: Lens selection - Part 3”. In: *Experimental Techniques* 37 (1 Jan. 2013), pp. 1–3. ISSN: 07328818. DOI: 10.1111/ext.12000.

[32] Phillip Reu. *Stereo-rig design: Lighting - Part 5*. May 2013. DOI: 10.1111/ext.12020.

[33] Phillip Reu. *Stereo-rig design: Stereo-angle selection - Part 4*. Mar. 2013. DOI: 10.1111/ext.12006.

[34] Matti Ristinmaa and Niels Saabye Ottosen. “The mechanics of constitutive modeling”. In: *Elsevier* (2005). DOI: 10.1016/B978-0-08-044606-6.X5000-0.

[35] Flaminio Cesar Sales et al. “Stress Concentration on PDMS: An evaluation of three numerical constitutive models using digital image correlation”. In: *Journal of the Mechanical Behavior of Biomedical Materials* 148 (2023), p. 106164. ISSN: 1751-6161. DOI: https://doi.org/10.1016/j.jmbbm.2023.106164. URL: https://www.sciencedirect.com/science/article/pii/S1751616123005179.

[36] M.A. Sutton and F. Hild. “Recent Advances and Perspectives in Digital Image Correlation”. In: *Experimental Mechanics* 55.1 (2015), pp. 1–8. DOI: 10.1007/s11340-015-9991-6.

[37] M.A. Sutton et al. “Advances in Two-Dimensional and Three-Dimensional Computer Vision”. In: *Photomechanics*. Ed. by P.K. Rastogi. Vol. 77. Topics in Applied Physics. Berlin, Heidelberg: Springer, 2000, pp. 323–372.

[38] M.A. Sutton et al. “Recent Progress in Digital Image Correlation: Background and Developments Since the 2013 W M Murray Lecture”. In: *Experimental Mechanics* 57.1 (2017), pp. 1–30. DOI: 10.1007/s11340-016-0233-3.

[39] Michael A. Sutton. “Digital Image Correlation for Shape and Deformation Measurements”. In: *Springer Handbook of Experimental Solid Mechanics*. Ed. by William N. Sharpe. Springer, 2008. Chap. 20, pp. 565–600. DOI: https://doi.org/10.1007/978-0-387-30877-7_20.

[40] Chenxu Wang and Roman Boulatov. “Autonomic Self-Healing of Polymers: Mechanisms, Applications, and Challenges”. In: *Molecules* 30.3 (2025). DOI: 10.3390/molecules30030469. URL: https://www.mdpi.com/1420-3049/30/3/469.

[41] Niamh Willis-Fox et al. “Polymer Mechanochemistry: Manufacturing Is Now a Force to Be Reckoned With”. In: *Chem* 4.11 (2018), pp. 2499–2537. ISSN: 2451-9294. DOI: https://doi.org/10.1016/j.chempr.2018.08.001. URL: https://www.sciencedirect.com/science/article/pii/S2451929418303280.

[42] M.R. Wisnom et al. “Mechanisms generating residual stresses and distortion during manufacture of polymer–matrix composite structures”. In: *Composites Part A: Applied Science and Manufacturing* 37.4 (2006). Internal Stresses in Polymer Composites, pp. 522–529. ISSN: 1359-835X. DOI: https://doi.org/10.1016/j.compositesa.2005.05.019. URL: https://www.sciencedirect.com/science/article/pii/S1359835X0500179X.

[43] Gao Hong Zhai et al. “A semiclassical molecular dynamics of the photochromic ring-opening reaction of spiropyran”. In: *Chinese Chemical Letters* 25 (5 2014), pp. 727–731. ISSN: 10018417. DOI: 10.1016/j.cclet.2014.01.050.

A

Methodology procedure

It is critical to ensure that it maintains an ease of understanding and continued use of the developed methodology, this appendix provides a user manual for the developed methodology. The preceding steps describe the physical preparation and acquisition process, the integration of multiple hardware components required a dedicated software environment to ensure synchronized operation. Presenting this software manual within the thesis is therefore essential, as it documents how the imaging, illumination, and mechanical systems were consolidated into a single user interface. This provides clarity on the implemented workflow and ensures reproducibility for future studies making use of the setup.

To begin the procedure, initialize the hardware. Turn on the Tenma power supply, the camera, and the computer, and connect the Arduino to the USB hub. Load Micro-Manager with the "BSI_arduino_input.cfg" file that contains the configuration for the hardware components. Proceed to load the sample:

Sample mounting

First, unscrew the sample mounts; there are two on the moving bed ($5.6\,\mathrm{mm}$ Allen key), one behind the load cell ($2.7\,\mathrm{mm}$ Allen key), and two on the fixed bed ($4.3\,\mathrm{mm}$ Allen key). Prepare the left bed with two layers of 3M double-sided adhesive tape on the bottom and one additional layer on top. Prepare the right bed similarly, and add a steel plate on the bottom for support. Position the sample with its patterned side facing downward on the right bed and screw it in. Attach the load cell at the back, and clamp the left bed. To distribute the forces evenly, tighten the screws gradually, alternating between the two.

For fluorescence-based visualization, use a glycerol–water mixture in a 73:27 ratio. This helps avoid glare by reducing light scattering at the hole boundary, as the mixture has a refractive index similar to PDMS. Apply the mixture to the bottom glass pane to secure it to the sample. Repeat for the top pane, ensuring minimal air bubbles are trapped. Handle the glass panes carefully: clean them with microfiber cloths and touch only the sides so that no dust, excess glycerol, fingerprints, or other contaminants obstruct the view. Verify the setup, then proceed to data acquisition.

Data acquisition
Carry out data acquisition using *Micro-Manager* and LabVIEW. In *Micro-Manager*, load the experimental script (`runtest.bsh`) through the Script Panel and define the test parameters. Use LabVIEW to run the loading sequence, record mechanical data, and save the output in real time. After both systems are initialized, start the experiment through the user interface, which consolidates control of all hardware components (see the following section).

A.1. Methodology: software Manual

The developed methodology includes a specialized user interface to consolidate the functionality of the stage, LEDs, and camera, allowing adaptability for future research using the setup. This integrates the Prime BSI CMOS camera, the Zaber translation stage (X-LRT0250HL-AE53C), as well as the Arduino

Uno R3, which manages the power to the two LEDs. To ensure all components work within Micro-Manager 2.0, a configuration file named “BSI_arduino_input.cfg” was created and is included in the supplementary materials. The goal of this section is to assist future work with a comprehensive user manual of the developed software.

After loading the correct configuration file for Micro-manager, the code can be accessed through “Tools > script panel > runtest.bsh”, if the correct file cannot be found, add it using the button on the top left corner of the script panel. Ensure that the correct ports are selected for the devices which can be done through “Devices_hardware configuration wizard”, a detailed guide on this can be found on the micromanager website.

At this stage, mount the sample, with the addition of a glycerol–water mixture. Double-click the code or press “Run” to launch the UI, as shown in Figure A.1.

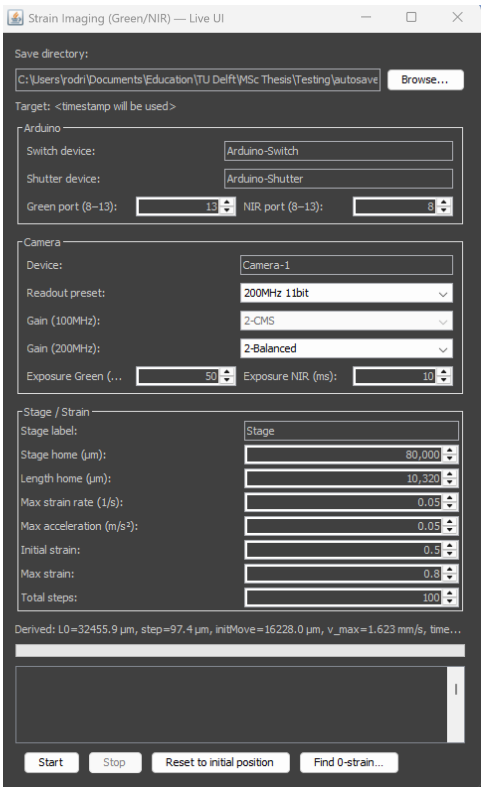

Figure A.1: User Interface for developed software

In the UI, the testing and hardware parameters can be set. The first box sets the Arduino output ports for the LEDs so that, if the hardware changes, the code can be adapted easily. The next box allows changes to camera parameters such as readout rate and related settings; more information is available in the Teledyne camera manual. Additionally, this section allows separate exposure per LED. For the green LED, an exposure of $800\,\mathrm{ms}$ was selected to allow full visualization of the fluorescence pattern; for the NIR LED, $5\,\mathrm{ms}$ was sufficient and avoided oversaturation. The following parameters were set: readout preset “100 MHz, 16-bit” and gain “1-HDR”.

The final box contains the stage parameters. The first two parameters, “Stage Home” and “Length Home,” should be adjusted only if the hardware is changed; they refer to the distance of the stage relative to its position on the bed. When changing these values, double-check the position with the Zaber Launcher software, which reports micrometer-level accuracy. The maximum strain rate and maximum acceleration limit the stage speed, while the actual strain rate is determined by the number of steps relative to the desired strain. The most important parameters are the final three: the initial strain and maximum strain, which determine the test range, and the total steps, which set the number of images.

Lastly, at the bottom of the UI, four buttons are available. “Start” and “Stop” initialize and interrupt the image sequence, respectively. “Reset to Initial Position” returns the sample to its original length. “Find 0-Strain” opens a prompt shown in Figure A.2; this determines the zero-load position of the load cell, with options to select fitted or threshold values—meaning, respectively, the position where the load cell reads 0 force or where the sample is flat.

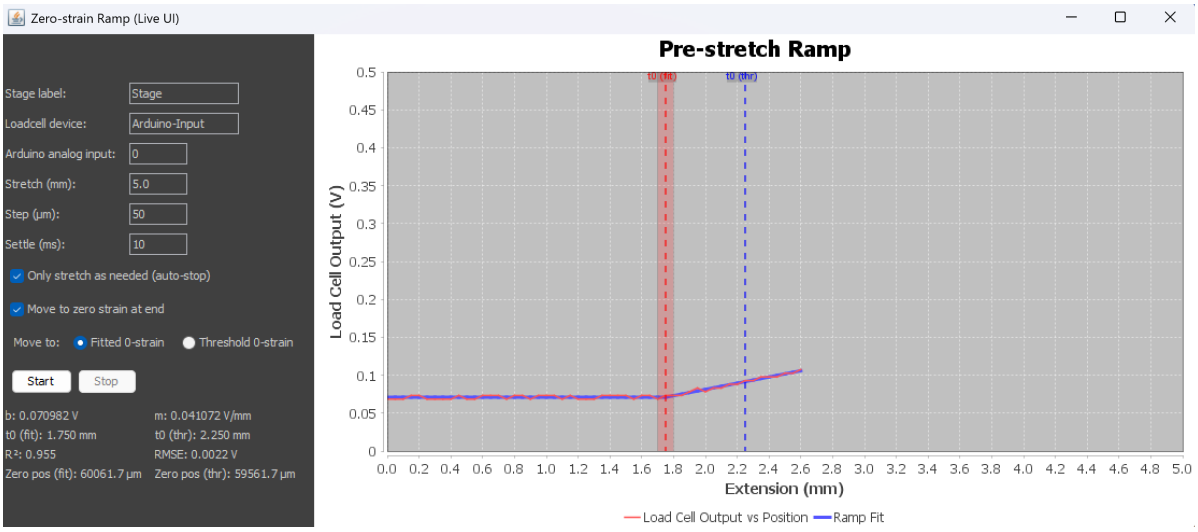

Figure A.2: Determine 0 strain position

B

Additional experimental set-up

This appendix describes the experimental set-up in detail, including the additional hardware used for dual-channel fluorescence imaging. It contains a schematic of the electrical components for switching between LEDs, as well as a complete list of parts with specifications, sources, and quantities. This information is provided so the set-up can be accurately reproduced.

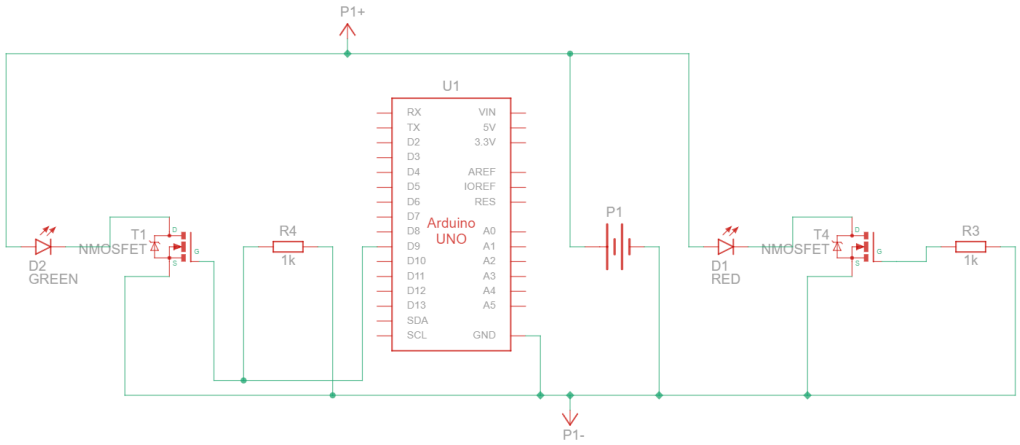

Figure B.1: Schematic view of added circuit

Name	Qty.	Component	Link
U1	1	Arduino Uno R3	nl.rs-online.com/web/p/arduino/7154081?gb=s
D2	1	Green LED	benl.rs-online.com/web/p/ir-leds/8777095
D1	1	Red LED	nl.rs-online.com/web/p/led-arrays/2269505
T1, T4	2	nMOS Transistor (MOSFET)	nl.rs-online.com/web/p/mosfets/5430074
R3, R4	2	10 kΩ Resistor	nl.rs-online.com/web/p/arduino/7617355?gb=s
P1	1	3.3 , 5V Power Supply	N/A
–	1	Breadboard	nl.rs-online.com/web/p/breadboards/0144717?gb=a

C

Relevant Codes

Code written in Beanshell ran through Micro-manager 2.0 responsible for operating the translating bed, image acquisition, alternating between green LED and NIR LED, as well as the synchronization of all steps to ensure smooth and consistent data acquisition.

```
// === Strain Imaging UI (camera presets fixed; gain tied to readout; daemon worker; save to TIFF) ===
// Rerun-safe globals
try { unset("STR_UI_FRAME"); } catch (Exception ignore) {}
try { unset("STR_runFlag"); } catch (Exception ignore) {}
try { unset("STR_workerRef"); } catch (Exception ignore) {}
try { unset("STR_store"); } catch (Exception ignore) {}
try { unset("STR_display"); } catch (Exception ignore) {}
try { unset("STR_cb"); } catch (Exception ignore) {}
try { unset("STR_initspeed"); } catch (Exception ignore) {}
try { unset("STR_initacc"); } catch (Exception ignore) {}
try { unset("STR_inittimeout"); } catch (Exception ignore) {}
try { unset("STR_initpos"); } catch (Exception ignore) {}
try { unset("STR_SCRIPTS_DIR"); } catch (Exception ignore) {}

// Imports
import java.awt.*;
import java.awt.event.*;
import javax.swing.*;
import javax.swing.border.*;
import java.io.File;
import java.text.SimpleDateFormat;
import java.util.Date;
import java.util.concurrent.atomic.AtomicBoolean;

import org.micromanager.data.Datastore;
import org.micromanager.data.Image;
import org.micromanager.data.Coords;
import org.micromanager.display.DisplayWindow;
import mmcorej.TaggedImage;

// ==== UI ====
JFrame STR_UI_FRAME = new JFrame("Strain Imaging (Green/NIR)   Live UI");
STR_UI_FRAME.setDefaultCloseOperation(JFrame.DISPOSE_ON_CLOSE);
STR_UI_FRAME.setLayout(new BorderLayout(8,8));

JPanel left = new JPanel(new GridBagLayout());
left.setBorder(new EmptyBorder(10,10,10,10));
GridBagConstraints gc = new GridBagConstraints();
gc.insets = new Insets(4,6,4,6);
gc.anchor = GridBagConstraints.WEST;
gc.fill = GridBagConstraints.HORIZONTAL;
gc.weightx = 1.0;

int row = 0;
```

```
45
46 // Script location - Change if device is changed
47 File STR_SCRIPTS_DIR = new File("C:/Users/rodri/Desktop");
48
49 // ===== Save ===== Change if device is changed
50 JTextField tfBaseDir = new JTextField("C:\\Users\\rodri\\Documents\\Education\\TU Delft\\MSc
       Thesis\\Testing\\autosave", 28);
51 JButton btnBrowse = new JButton("Browse...");
52 JLabel lblSaveAs  = new JLabel("Target: <timestamp will be used>");
53 {
54     gc.gridx=0; gc.gridy=row; left.add(new JLabel("Save directory:"), gc);
55     JPanel dirLine = new JPanel(new BorderLayout(6,0));
56     dirLine.add(tfBaseDir, BorderLayout.CENTER);
57     dirLine.add(btnBrowse, BorderLayout.EAST);
58     gc.gridx=0; gc.gridy=++row; left.add(dirLine, gc);
59     gc.gridx=0; gc.gridy=++row; left.add(lblSaveAs, gc);
60 }
61
62 // ===== Arduino (devices + LED pins 8 13) =====
63 JTextField tfSwitchDev = new JTextField("Arduino-Switch", 14);
64 JTextField tfShutDev   = new JTextField("Arduino-Shutter", 14);
65 JSpinner spGreenPort   = new JSpinner(new SpinnerNumberModel(13, 8, 13, 1));
66 JSpinner spNIRPort     = new JSpinner(new SpinnerNumberModel(8,  8, 13, 1));
67 spGreenPort.setEditor(new JSpinner.NumberEditor(spGreenPort, "0"));
68 spNIRPort.setEditor(new JSpinner.NumberEditor(spNIRPort, "0"));
69 {
70     JPanel p = new JPanel(new GridBagLayout());
71     p.setBorder(new TitledBorder("Arduino"));
72     GridBagConstraints agc = new GridBagConstraints();
73     agc.insets = new Insets(4,6,4,6);
74     agc.anchor = GridBagConstraints.WEST;
75     agc.fill   = GridBagConstraints.HORIZONTAL;
76     agc.weightx = 1.0;
77     int ar = 0;
78
79     agc.gridx=0; agc.gridy=ar; p.add(new JLabel("Switch device:"), agc);
80     agc.gridx=1;               p.add(tfSwitchDev, agc);
81
82     agc.gridx=0; agc.gridy=++ar; p.add(new JLabel("Shutter device:"), agc);
83     agc.gridx=1;                 p.add(tfShutDev, agc);
84
85     JPanel pins = new JPanel(new GridLayout(1,4,8,0));
86     pins.add(new JLabel("Green port (8 13):")); pins.add(spGreenPort);
87     pins.add(new JLabel("NIR port (8 13):"));   pins.add(spNIRPort);
88
89     agc.gridx=0; agc.gridy=++ar; agc.gridwidth=2; p.add(pins, agc);
90     agc.gridwidth=1;
91
92     gc.gridx=0; gc.gridy=++row; left.add(p, gc);
93 }
94
95 // Camera (fixed presets)
96 JTextField tfCameraDev = new JTextField("Camera-1", 12);
97
98 // Readout preset
99 String[] READOUT_PRESETS = new String[]{ "200MHz 11bit", "100MHz 16bit" };
100 JComboBox cbReadout = new JComboBox(READOUT_PRESETS);
101
102 // Gain presets per readout
103 String[] GAIN_200 = new String[]{ "1-Full well", "2-Balanced", "3-Sensitivity" };
104 String[] GAIN_100 = new String[]{ "1-HDR", "2-CMS" };
105 JComboBox cbGain200 = new JComboBox(GAIN_200);
106 JComboBox cbGain100 = new JComboBox(GAIN_100);
107
108 // Camera presets
109 cbReadout.setSelectedItem("200MHz 11bit");
110 cbGain100.setSelectedItem("2-CMS");
111 cbGain100.setEnabled(false);
112 cbGain200.setSelectedItem("2-Balanced");
113 cbGain200.setEnabled(true);
114
```

```
JSpinner spExposureGreen = new JSpinner(new SpinnerNumberModel(50.0, 1.0, 10000.0, 1.0));
JSpinner spExposureNIR   = new JSpinner(new SpinnerNumberModel(10.0, 1.0, 10000.0, 1.0));

{
    JPanel p = new JPanel(new GridBagLayout());
    p.setBorder(new TitledBorder("Camera"));
    GridBagConstraints cgc = new GridBagConstraints();
    cgc.insets = new Insets(4,6,4,6);
    cgc.anchor = GridBagConstraints.WEST;
    cgc.fill   = GridBagConstraints.HORIZONTAL;
    cgc.weightx = 1.0;
    int cr = 0;

    cgc.gridx=0; cgc.gridy=cr; p.add(new JLabel("Device:"), cgc);
    cgc.gridx=1;               p.add(tfCameraDev, cgc);

    cgc.gridx=0; cgc.gridy=++cr; p.add(new JLabel("Readout preset:"), cgc);
    cgc.gridx=1;                 p.add(cbReadout, cgc);

    cgc.gridx=0; cgc.gridy=++cr; p.add(new JLabel("Gain (100MHz):"), cgc);
    cgc.gridx=1;                 p.add(cbGain100, cgc);

    cgc.gridx=0; cgc.gridy=++cr; p.add(new JLabel("Gain (200MHz):"), cgc);
    cgc.gridx=1;                 p.add(cbGain200, cgc);

    // Two exposures
  JPanel expRow = new JPanel(new GridLayout(1, 4, 8, 0));
  expRow.add(new JLabel("Exposure Green (ms):"));
  expRow.add(spExposureGreen);
  expRow.add(new JLabel("Exposure NIR (ms):"));
  expRow.add(spExposureNIR);

  cgc.gridx = 0; cgc.gridy = ++cr; cgc.gridwidth = 2; // span the two columns of 'p'
  p.add(expRow, cgc);
  cgc.gridwidth = 1; // reset for following rows

    cbReadout.addActionListener(new ActionListener(){ public void actionPerformed(ActionEvent
     e){
        boolean is200 = "200MHz 11bit".equals(cbReadout.getSelectedItem());
        cbGain200.setEnabled(is200);
        cbGain100.setEnabled(!is200);
    }});

    gc.gridx=0; gc.gridy=++row; left.add(p, gc);
}


// ===== Stage & strain =====
JTextField tfStage     = new JTextField("Stage", 10);
JSpinner spStageHome   = new JSpinner(new SpinnerNumberModel(80000.0, 0, 250000.0, 100.0));
    // µm 202000.0
JSpinner spLengthHome  = new JSpinner(new SpinnerNumberModel(10320.0, 0, 50000, 10.0));  //
    µm   21540.0
JSpinner spMaxSR       = new JSpinner(new SpinnerNumberModel(0.05, 0.0001, 10.0, 0.01));   //
     1/s
JSpinner spMaxAcc      = new JSpinner(new SpinnerNumberModel(0.05, 0.0001, 10.0, 0.01));   //
     m/s^2
JSpinner spStrainInit  = new JSpinner(new SpinnerNumberModel(0.5, 0.0, 10.0, 0.01));
JSpinner spStrainMax   = new JSpinner(new SpinnerNumberModel(0.8, 0.0, 10.0, 0.01));
JSpinner spSteps       = new JSpinner(new SpinnerNumberModel(100, 1, 100000, 1));
{
    JPanel p = new JPanel(new GridLayout(8,2,8,4));
    p.setBorder(new TitledBorder("Stage / Strain"));
    p.add(new JLabel("Stage label:"));           p.add(tfStage);
    p.add(new JLabel("Stage home (µm):"));       p.add(spStageHome);
    p.add(new JLabel("Length home (µm):"));      p.add(spLengthHome);
    p.add(new JLabel("Max strain rate (1/s):")); p.add(spMaxSR);
    p.add(new JLabel("Max acceleration (m/s²):")); p.add(spMaxAcc);
    p.add(new JLabel("Initial strain:"));         p.add(spStrainInit);
    p.add(new JLabel("Max strain:"));             p.add(spStrainMax);
    p.add(new JLabel("Total steps:"));            p.add(spSteps);
```

```
181
182     gc.gridx=0; gc.gridy=++row; left.add(p, gc);
183 }
184
185 // ===== Derived & status =====
186 JLabel lblDerived = new JLabel("Derived: L0=?, step=?, initMove=?, v_max=?, timeout=? ms");
187 JProgressBar prog = new JProgressBar(0, 100);
188
189 // Wider, taller log with wrapping
190 JTextArea log = new JTextArea(18, 70);        // was (12, 40)
191 log.setLineWrap(true);
192 log.setWrapStyleWord(true);
193 // Optional: monospaced is nice for aligned messages
194 // log.setFont(new java.awt.Font("Monospaced", java.awt.Font.PLAIN, 12));
195
196 JScrollPane logScroll = new JScrollPane(log);
197 logScroll.setPreferredSize(new Dimension(800, 300));  // ensure a roomy default
198
199 {
200     gc.gridx=0; gc.gridy=++row; gc.weightx=1.0; gc.fill=GridBagConstraints.HORIZONTAL;
201     left.add(lblDerived, gc);
202
203     gc.gridx=0; gc.gridy=++row; gc.weightx=1.0; gc.fill=GridBagConstraints.HORIZONTAL;
204     left.add(prog, gc);
205
206     // Let the log consume remaining vertical space
207     gc.gridx=0; gc.gridy=++row;
208     gc.weightx=1.0;
209     gc.weighty=1.0;
210     gc.fill=GridBagConstraints.BOTH;
211     left.add(logScroll, gc);
212
213     // Reset for subsequent rows (e.g., the control buttons)
214     gc.weighty=0.0;
215     gc.fill=GridBagConstraints.HORIZONTAL;
216 }
217
218
219 // ===== Controls =====
220 JButton btnStart = new JButton("Start");
221 JButton btnStop  = new JButton("Stop"); btnStop.setEnabled(false);
222 JButton btnReset = new JButton("Reset to initial position");
223 JButton btnFind0 = new JButton("Find 0-strain ");
224 {
225     JPanel p = new JPanel(new FlowLayout(FlowLayout.LEFT, 8,0));
226     p.add(btnStart); p.add(btnStop); p.add(btnReset); p.add(btnFind0);
227     gc.gridx=0; gc.gridy=++row; left.add(p, gc);
228 }
229
230 STR_UI_FRAME.add(left, BorderLayout.CENTER);
231 STR_UI_FRAME.setMinimumSize(new Dimension(500, 800));
232 STR_UI_FRAME.setLocationByPlatform(true);
233 STR_UI_FRAME.setVisible(true);
234 STR_UI_FRAME.setSize(new Dimension(500, 800));
235
236
237 // ==== STATE & HELPERS ====
238 AtomicBoolean STR_runFlag = new AtomicBoolean(false);
239 Thread[] STR_workerRef = new Thread[1];
240
241 Datastore STR_store = null;
242 DisplayWindow STR_display = null;
243 Coords.Builder STR_cb = null;
244
245 String STR_initspeed = null;
246 String STR_initacc = null;
247 int    STR_inittimeout = 0;
248 double STR_initpos = 0.0;
249
250 void _log(String s) {
251     SwingUtilities.invokeLater(new Runnable(){ public void run(){
```

```
        log.append(s + "\n");
        log.setCaretPosition(log.getDocument().getLength());
    }});
}

String ts() { return new SimpleDateFormat("yyyyMMdd_HHmmss").format(new Date()); }

int arduinoMask(int port){
    if (port < 8 || port > 13) throw new IllegalArgumentException("Port must be 8..13");
    return 1 << (port - 8); // 8->1, 9->2,  , 13->32
}

// Browse: keep OS path verbatim
btnBrowse.addActionListener(new ActionListener(){ public void actionPerformed(ActionEvent e){
    JFileChooser ch = new JFileChooser(new File(tfBaseDir.getText()));
    ch.setFileSelectionMode(JFileChooser.DIRECTORIES_ONLY);
    int rv = ch.showOpenDialog(STR_UI_FRAME);
    if (rv == JFileChooser.APPROVE_OPTION) {
        tfBaseDir.setText(ch.getSelectedFile().getAbsolutePath());
    }
}});

// quick derived preview
Runnable updateDerived = new Runnable() {
    public void run() {
        try {
            String stage = tfStage.getText().trim();
            double stage_home   = ((Double)spStageHome.getValue()).doubleValue();
            double length_home  = ((Double)spLengthHome.getValue()).doubleValue();
            double maxSR        = ((Double)spMaxSR.getValue()).doubleValue();
            double maxAcc       = ((Double)spMaxAcc.getValue()).doubleValue();
            double strain_init  = ((Double)spStrainInit.getValue()).doubleValue();
            double strain_max   = ((Double)spStrainMax.getValue()).doubleValue();
            int    totalSteps   = ((Integer)spSteps.getValue()).intValue();

            double initpos = mmc.getPosition(stage);
            double L0 = length_home + (stage_home - initpos);   // µm
            double v_max = (maxSR * L0) / 1000.0;               // mm/s

            double strain_step = (strain_max - strain_init) / (double) totalSteps;
            double stepDistance = strain_step * L0;             // µm
            double initMove = strain_init * L0;                 // µm

            double a_um = maxAcc * 1e6;                         // µm/s²
            double v_um = v_max * 1e3;                          // µm/s
            double t_accel, d_accel, t_cruise;

            if (initMove > 0) {
                double d_accel_needed = (v_um*v_um) / (2*a_um);
                if (initMove > 2 * d_accel_needed) {
                    t_accel  = v_um / a_um;
                    d_accel  = d_accel_needed;
                    t_cruise = (initMove - 2*d_accel) / v_um;
                } else {
                    t_accel  = Math.sqrt(initMove / a_um);
                    d_accel  = 0.5 * a_um * t_accel * t_accel;
                    t_cruise = 0;
                }
            } else { t_accel=0; d_accel=0; t_cruise=0; }

            double initMoveTime = 2*t_accel + t_cruise;
            int timeoutms = (int)Math.ceil(initMoveTime * 1000 * 1.2);

            lblDerived.setText(String.format("Derived: L0=%.1f µm, step=%.1f µm, initMove=%.1
    f µm, v_max=%.3f mm/s, timeout=%d ms",
                new Object[]{ new Double(L0), new Double(stepDistance), new Double(initMove),
     new Double(v_max), new Integer(timeoutms)}));
        } catch (Exception ex) {
            lblDerived.setText("Derived:   (stage must be connected)");
        }
    }
```

```
};
updateDerived.run();

// Reset to initial position (no absolute move)
btnReset.addActionListener(new ActionListener(){ public void actionPerformed(ActionEvent e){
    new Thread(new Runnable(){ public void run(){
        try {
            String stage = tfStage.getText().trim();
            if (Double.isNaN(STR_initpos) || STR_initpos == 0.0) {
                _log("Reset skipped: initial position not set yet (run Start first).");
                return;
            }
            _log("Reset: moving stage to initial position: " + STR_initpos + " µm");
            mmc.setPosition(stage, STR_initpos);
            mmc.waitForDevice(stage);
            _log("Reset done.");
        } catch (Exception ex) {
            _log("Reset failed: " + ex);
        }
    }}, "ResetStage").start();
}});

// ===== START =====
btnStart.addActionListener(new ActionListener(){
    public void actionPerformed(ActionEvent e){
        if (STR_runFlag.get()) return;
        STR_runFlag.set(true);
        btnStart.setEnabled(false);
        btnStop.setEnabled(true);
        prog.setValue(0);
        updateDerived.run();

        Thread worker = new Thread(new Runnable(){ public void run(){
            try {
                // ---- Prepare save FILE (MULTIPAGE_TIFF needs a file path, not a folder)
    ----
          File baseDir = new File(tfBaseDir.getText().trim());
          if (!baseDir.isAbsolute()) baseDir = baseDir.getAbsoluteFile();
          baseDir = baseDir.toPath().normalize().toFile();

          // ensure the base folder exists
          if (!baseDir.exists()) baseDir.mkdirs();

          String baseName = ts();                       // e.g. 20250813_142233
          File outFile    = new File(baseDir, baseName);

          // avoid collisions (in case you rerun within the same second)
          int idx = 1;
          while (outFile.exists() || outFile.isDirectory()) {
              outFile = new File(baseDir, baseName + "_" + (idx++));
          }

          final String savePath = outFile.getAbsolutePath();
          SwingUtilities.invokeLater(new Runnable(){ public void run(){
              lblSaveAs.setText("Target: " + savePath);
          }});
          _log(">>> Will save MultiPage TIFF to file: " + savePath);


                // ---- Read UI ----
                String arduinoswitch  = tfSwitchDev.getText().trim();
                String arduinoshutter = tfShutDev.getText().trim();
                int greenPort = ((Integer)spGreenPort.getValue()).intValue();
                int NIRPort   = ((Integer)spNIRPort.getValue()).intValue();
                if (greenPort < 8 || greenPort > 13 || NIRPort < 8 || NIRPort > 13) {
                    JOptionPane.showMessageDialog(STR_UI_FRAME, "Ports must be in 8..13.", "
    Invalid port", JOptionPane.ERROR_MESSAGE);
                    STR_runFlag.set(false);
                    SwingUtilities.invokeLater(new Runnable(){ public void run(){ btnStart.
    setEnabled(true); btnStop.setEnabled(false); }});
                    return;
```

```
                }
                int greenCode = arduinoMask(greenPort);
                int NIRCode   = arduinoMask(NIRPort);

                String camera = tfCameraDev.getText().trim();
                String readoutPreset = (String) cbReadout.getSelectedItem();
                boolean is200 = "200MHz 11bit".equals(readoutPreset);
                String gainPreset = is200 ? (String)cbGain200.getSelectedItem() : (String)
    cbGain100.getSelectedItem();

                double exposureGreen = ((Double)spExposureGreen.getValue()).doubleValue();
            double exposureNIR   = ((Double)spExposureNIR.getValue()).doubleValue();

                String stage = tfStage.getText().trim();
                double stage_home   = ((Double)spStageHome.getValue()).doubleValue();
                double length_home  = ((Double)spLengthHome.getValue()).doubleValue();
                double maxSR        = ((Double)spMaxSR.getValue()).doubleValue();
                double maxAcc       = ((Double)spMaxAcc.getValue()).doubleValue();
                double strain_init  = ((Double)spStrainInit.getValue()).doubleValue();
                double strain_max   = ((Double)spStrainMax.getValue()).doubleValue();
                int    totalSteps   = ((Integer)spSteps.getValue()).intValue();

                // ---- Derived ----
                STR_initpos = mmc.getPosition(stage);
                double L0 = length_home + (stage_home - STR_initpos); // µm
                double maxspeed = (maxSR * L0) / 1000.0;              // mm/s
                double strain_step = (strain_max - strain_init) / (double) totalSteps;
                double stepDistance = strain_step * L0;               // µm
                double initMove = strain_init * L0;                   // µm

                double a_um = maxAcc * 1e6;
                double v_um = maxspeed * 1e3;
                double d_accel_needed = (v_um*v_um) / (2*a_um);
                double t_accel = (initMove > 2*d_accel_needed) ? (v_um / a_um) : Math.sqrt(
    initMove / a_um);
                double d_accel = (initMove > 2*d_accel_needed) ? d_accel_needed : (0.5 * a_um
     * t_accel * t_accel);
                double t_cruise = (initMove > 2*d_accel_needed) ? ((initMove - 2*d_accel) /
    v_um) : 0.0;
                double initMoveTime = 2*t_accel + t_cruise;
                int timeoutms = (int)Math.ceil(initMoveTime * 1000 * 1.2);

                _log(">>> Saving to: " + savePath);
                _log(String.format("Derived: L0=%.1f µm, step=%.1f µm, initMove=%.1f µm, vmax
    =%.3f mm/s, timeout=%d ms",
                    new Object[]{ new Double(L0), new Double(stepDistance), new Double(
    initMove), new Double((maxSR*L0)/1000.0), new Integer(timeoutms)}));

                // ---- Remember settings ----
                STR_initspeed   = mmc.getProperty(stage, "Speed [mm/s]");
                STR_initacc     = mmc.getProperty(stage, "Acceleration [m/s^2]");
                STR_inittimeout = mmc.getTimeoutMs();

                // ---- Datastore & display ----
                STR_cb = mm.data().getCoordsBuilder().z(0).p(0);
                STR_store = mm.data().createRAMDatastore();
                STR_display = mm.displays().createDisplay(STR_store);

                // ---- Apply camera configs (no free-typing; only selected pair) ----
                // 1) Readout group (usually "Readout Rate")
                try {
                    mmc.setConfig("Readout Rate", readoutPreset);
                    mmc.waitForConfig("Readout Rate", readoutPreset);
                } catch (Exception ex1) {
                    _log("Warning: could not set 'Readout Rate' to '" + readoutPreset + "': "
     + ex1);
                }

                // 2) Gain group tied to readout
                String gainGroup = is200 ? "200 MHz Gain" : "100 MHz Gain";
                boolean applied = false;
```

```
453                 try {
454                     mmc.setConfig(gainGroup, gainPreset);
455                     mmc.waitForConfig(gainGroup, gainPreset);
456                     applied = true;
457                 } catch (Exception ex2) {
458                     // Fallback to names without space if your config uses "200MHz Gain"/"100
    MHz Gain"
459                     String alt = is200 ? "200MHz Gain" : "100MHz Gain";
460                     try {
461                         mmc.setConfig(alt, gainPreset);
462                         mmc.waitForConfig(alt, gainPreset);
463                         applied = true;
464                     } catch (Exception ex3) {
465                         _log("Warning: could not set gain group '" + gainGroup + "' or '" +
    alt + "' to '" + gainPreset + "'.");
466                     }
467                 }
468 
469                 mmc.setProperty(stage, "Speed [mm/s]", maxspeed);
470                 mmc.setProperty(stage, "Acceleration [m/s^2]", maxAcc);
471                 mmc.setTimeoutMs(timeoutms);
472 
473                 // ---- Initial move ----
474                 try {
475                     _log(String.format("Moving to initial strain (%.0f µm)   ~%d s", new
    Object[]{ new Double(initMove), new Integer((int)Math.round(initMoveTime))}));
476                     mmc.setPosition(stage, STR_initpos - initMove); // negative pulls
477                     mmc.waitForDevice(stage);
478                     _log("Reached: " + mmc.getPosition(stage) + " µm");
479                 } catch (Exception ex) {
480                     _log("Initial move failed: " + ex);
481                 } finally {
482                     mmc.setTimeoutMs(STR_inittimeout); // restore timeout before loop
483                 }
484 
485                 // ---- Acquisition loop ----
486                 prog.setMaximum(totalSteps);
487                 for (int step = 0; step < totalSteps && STR_runFlag.get() && !Thread.
    currentThread().isInterrupted(); step++) {
488                     double targetPos = STR_initpos - initMove - step * stepDistance;
489 
490                     try { mmc.setPosition(stage, targetPos); mmc.waitForDevice(stage); }
491                     catch (Exception ex) { _log("Stage move failed at step " + step + ": " +
    ex); }
492 
493                     // Green
494                 try {
495                     mmc.setProperty(camera, "Exposure", exposureGreen);
496                     mmc.setProperty(arduinoswitch, "State", greenCode);
497                     mmc.setProperty(arduinoshutter, "OnOff", 1);
498                     mmc.snapImage();
499                     TaggedImage ti = mmc.getTaggedImage();
500                     Coords c = STR_cb.t(step).c(0).build();
501                     Image im = mm.data().convertTaggedImage(ti, c, null);
502                     STR_store.putImage(im);
503                 } catch (Exception ex) { _log("Green snap failed at step " + step + ": " + ex);
     }
504 
505                 // NIR
506                 try {
507                     mmc.setProperty(camera, "Exposure", exposureNIR);
508                     mmc.setProperty(arduinoswitch, "State", NIRCode);
509                     mmc.setProperty(arduinoshutter, "OnOff", 1);
510                     mmc.snapImage();
511                     TaggedImage ti2 = mmc.getTaggedImage();
512                     Coords c2 = STR_cb.t(step).c(1).build();
513                     Image im2 = mm.data().convertTaggedImage(ti2, c2, null);
514                     STR_store.putImage(im2);
515                 } catch (Exception ex) { _log("NIR snap failed at step " + step + ": " + ex); }
516 
517 
```

```
518                     // shutter off between steps
519                     // try { mmc.setProperty(arduinoshutter, "OnOff", 0); } catch (Exception
    ignore) {}
520
521                     final int fStep = step+1;
522                     SwingUtilities.invokeLater(new Runnable(){ public void run(){ prog.
    setValue(fStep); }});
523                 }
524
525                 _log("Acquisition loop finished.");
526
527             // ---- Save ----
528             try {
529                 if (STR_store != null && !STR_store.isFrozen()) STR_store.freeze();
530                 STR_store.save(Datastore.SaveMode.MULTIPAGE_TIFF, savePath);  // savePath is
    the .tif file
531                 _log("Saved MultiPage TIFF to: " + savePath);
532             } catch (Exception ex) {
533                 _log("Saving failed: " + ex);
534             }
535
536
537
538             } catch (Exception exOuter) {
539                 _log("Fatal error: " + exOuter);
540             } finally {
541                 // ---- Shutdown / restore ----
542                 try { mmc.setProperty(tfSwitchDev.getText().trim(), "State", 0); } catch (
    Exception ignore) {}
543                 try { mmc.setProperty(tfShutDev.getText().trim(), "OnOff", 0); } catch (
    Exception ignore) {}
544
545                 try { mmc.setTimeoutMs(STR_inittimeout); } catch (Exception ignore) {}
546                 try { mmc.setProperty(tfStage.getText().trim(), "Speed [mm/s]", STR_initspeed
    ); } catch (Exception ignore) {}
547                 try { mmc.setProperty(tfStage.getText().trim(), "Acceleration [m/s^2]",
    STR_initacc); } catch (Exception ignore) {}
548
549               //  try {
550               //      _log("Returning stage to initial position: " + STR_initpos + " µm");
551               //      mmc.setPosition(tfStage.getText().trim(), STR_initpos);
552               //      mmc.waitForDevice(tfStage.getText().trim());
553               //  } catch (Exception ex) { _log("Failed to return stage: " + ex); }
554
555                 STR_runFlag.set(false);
556                 SwingUtilities.invokeLater(new Runnable(){ public void run(){ btnStart.
    setEnabled(true); btnStop.setEnabled(false); }});
557             }
558         }}, "StrainWorker");
559         worker.setDaemon(true);
560         STR_workerRef[0] = worker;
561         worker.start();
562     }
563 });
564
565 // ===== STOP =====
566 btnStop.addActionListener(new ActionListener(){ public void actionPerformed(ActionEvent e){
567     STR_runFlag.set(false);
568     try { if (STR_workerRef[0] != null && STR_workerRef[0].isAlive()) STR_workerRef[0].
    interrupt(); } catch (Exception ignore) {}
569     btnStop.setEnabled(false);
570     _log("Stop requested.");
571 }});
572
573 // ===== Window close cleanup =====
574 Runnable cleanup = new Runnable(){ public void run(){
575     STR_runFlag.set(false);
576     try { if (STR_workerRef[0] != null && STR_workerRef[0].isAlive()) STR_workerRef[0].
    interrupt(); } catch (Exception ignore) {}
577
```

```
578     try { mmc.setProperty(tfSwitchDev.getText().trim(), "State", 0); } catch (Exception
        ignore) {}
579     try { mmc.setProperty(tfShutDev.getText().trim(), "OnOff", 0); } catch (Exception ignore)
         {}
580     try { mmc.setTimeoutMs(STR_inittimeout); } catch (Exception ignore) {}
581     try { mmc.setProperty(tfStage.getText().trim(), "Speed [mm/s]", STR_initspeed); } catch (
        Exception ignore) {}
582     try { mmc.setProperty(tfStage.getText().trim(), "Acceleration [m/s^2]", STR_initacc); }
        catch (Exception ignore) {}
583
584     try { STR_UI_FRAME.dispose(); } catch (Exception ignore) {}
585 }};
586 STR_UI_FRAME.addWindowListener(new WindowAdapter(){ public void windowClosing(WindowEvent e){
         cleanup.run(); }});
587
588 // ---- Find 0-strain button: search & verbose logging, remember folder ----
589 btnFind0.addActionListener(new ActionListener(){ public void actionPerformed(ActionEvent e){
590     new Thread(new Runnable(){ public void run(){
591         try {
592             final String defaultName = "find0strain.bsh";
593
594             // Candidates: remembered scripts dir ? working dir ? save dir
595             File scriptsDir = (STR_SCRIPTS_DIR != null) ? STR_SCRIPTS_DIR : new File(".").
        getAbsoluteFile();
596             File workDir    = new File(".").getAbsoluteFile();
597             File saveDir    = new File(tfBaseDir.getText().trim());
598
599             File candidateA = new File(scriptsDir, defaultName);
600             File candidateB = new File(workDir,  defaultName);
601             File candidateC = new File(saveDir,  defaultName);
602
603             File target = null;
604             if (candidateA.exists() && candidateA.isFile()) target = candidateA;
605             else if (candidateB.exists() && candidateB.isFile()) target = candidateB;
606             else if (candidateC.exists() && candidateC.isFile()) target = candidateC;
607
608             if (target == null) {
609                 _log("find0: none found; opening chooser at: " + describe(scriptsDir));
610                 final File[] sel = new File[1];
611                 try {
612                     javax.swing.SwingUtilities.invokeAndWait(new Runnable(){ public void run
        (){
613                         JFileChooser ch = new JFileChooser(scriptsDir);
614                         ch.setDialogTitle("Select find0strain.bsh");
615                         ch.setFileSelectionMode(JFileChooser.FILES_ONLY);
616                         int rv = ch.showOpenDialog(STR_UI_FRAME);
617                         if (rv == JFileChooser.APPROVE_OPTION) sel[0] = ch.getSelectedFile();
618                     }});
619                 } catch (Exception edtEx) { _log("find0: chooser error: " + edtEx); }
620                 if (sel[0] == null) { _log("Find 0-strain canceled."); return; }
621                 target = sel[0];
622                 // remember folder for next time
623                 try { STR_SCRIPTS_DIR = target.getAbsoluteFile().getParentFile(); } catch (
        Throwable t) {}
624                 _log("find0: remembered STR_SCRIPTS_DIR = " + describe(STR_SCRIPTS_DIR));
625             }
626
627             String path = target.getAbsolutePath();
628             _log("Launching find0strain: " + path);
629
630             // Run in a fresh interpreter; pass mm & mmc
631             try {
632                 bsh.Interpreter it = new bsh.Interpreter();
633                 it.set("mm", mm);
634                 it.set("mmc", mmc);
635                 it.source(path);
636                 _log("find0strain completed.");
637             } catch (Throwable ex2) {
638                 javax.swing.SwingUtilities.invokeLater(new Runnable(){ public void run(){
639                     JOptionPane.showMessageDialog(STR_UI_FRAME,
640                         "Could not run find0strain:\\n" + path + "\\n" + ex2,
```

```
                        "findOstrain", JOptionPane.ERROR_MESSAGE);
                });
            }
        } catch (Throwable ex) {
            _log("findOstrain launch failed: " + ex);
        }
    }, "RunFindOStrain").start();
});
```